On the stick-slip flow from slit and cylindrical dies of a Phan-Thien and Tanner fluid model. I. Steady state

George Karapetsas and John Tsamopoulos[a)]
Department of Chemical Engineering, Laboratory of Computational Fluid Dynamics, University of Patras, Patras 26500, Greece

(Received 28 April 2009; accepted 13 November 2009; published online 8 December 2009)

The steady planar and cylindrical stick-slip flows for a viscoelastic fluid are computed using the Phan-Thien and Tanner (PTT) constitutive model. The mixed finite element method is used in combination with the elastic-viscous stress-splitting technique and the streamline upwind Petrov–Galerkin discretization for the constitutive equation. This combination of methods when applied to the PTT constitutive model allows us to compute steady state solutions up to high Weissenberg numbers; practically without an upper limit. Equally important, the global Jacobian matrix is generated in order to be able to perform a linear stability analysis of the computed steady state. The dependence of the steady solutions on all the problem parameters is examined. In the limit of a Newtonian fluid, the expansion coefficients near the singularity are computed with comparable accuracy to those from previous analytical and numerical studies, which include the singular finite element method. In the case of a viscoelastic liquid, it is shown that the computed solutions converge quadratically with mesh refinement even at the exit plane of the die and also locally very close to the singularity. The form of the converged solution near the singularity is examined as well as its dependence on various rheological parameters. It is shown that the singularity at the die exit is a logarithmic one and always integrable. Under such conditions our calculations can be extended to determine the linear stability of the herein computed steady states. © *2009 American Institute of Physics*. [doi:10.1063/1.3271495]

I. INTRODUCTION

Most polymer processing operations involve, at some stage, extrusion of viscoelastic fluids from dies of various shapes. This fact makes extrusion studies so important that numerous experimental and theoretical studies have been undertaken,[1–4] trying to increase our understanding of the very complex behavior of an array of polymers being extruded from a variety of dies under different conditions. Unfortunately, very important technical questions still remain. Extrusion is particularly complicated because it involves (a) an abrupt change from boundary conditions on the velocity inside the die to boundary conditions on the stress outside it, making the point of departure from the die a mathematically singular one; (b) a swelling of the extrudate that can be even more than ten times larger if a viscoelastic material is involved, instead of a Newtonian fluid; (c) various morphological deformations that arise on the extrudate interface or its bulk. The latter introduce severe limitations on extrusion rates, if product quality is to be maintained.

Although the proposed mechanisms leading to these deformations are very different in principle, it is very difficult to distinguish their effect in practice. This is exactly the aspect where a theoretical approach could play an important role in order to improve our understanding of the extrusion process. This is the ultimate goal of our work and in order to achieve this, we decided:

(a) To work with the simplest possible flow arrangement that retained the abrupt change in the boundary conditions from no slip along the wall to perfect slip along the free surface where experiments have indicated that surface instabilities are initiated, without the complication of an unknown free surface: the stick-slip flow. This is an important special case of extrusion flows from dies since it is formally equivalent to the free surface problem in the limit of infinite surface tension, where the normal stress balance reduces to the equation of zero curvature in the flow direction.

(b) To avoid using slip along the die wall and use a constitutive law which is able to predict the main flow properties of polymeric fluids with monotonic flow curves. Such a model is the affine Phan-Thien and Tanner (PTT) model,[5,6] which is based on network theory. With only one additional parameter to fluid elasticity and viscosity, it can predict a finite extensional viscosity which is extensional hardening with increasing extension rate followed by either a constant extensional viscosity (in the linear version of the model) or extensional thinning (in its exponential version) and shear thinning. All these effects are observed in the majority of viscoelastic fluids.

We will begin our presentation with a short description of our code making sure that its predictions converge with mesh refinement and that the expected singularity is integrable for the parameters used before performing a thorough examination of the steady viscoelastic stick-slip flow. This

[a)]Author to whom correspondence should be addressed. Electronic mail: tsamo@chemeng.upatras.gr. Fax: +(30) 2610-996-178.

will be followed by a linear stability analysis around this base state, which is the subject of part II of this paper, to find out whether flow instabilities can be predicted. This is a classical method that has been applied with success in the past to examine the stability of numerous problems of both Newtonian and non-Newtonian fluid flows,[7,8] but it is quite strange that it has not been undertaken in extrusion flows.

The simplification of a fixed fluid boundary, introduced in the stick-slip flow, eliminates the nonlinearity in the extrusion of a Newtonian fluid and Richardson[9] was the first to be able to find an analytical solution to the planar stick-slip problem using the Wiener–Hopf method. However the strength of the singularity that was predicted is incorrect as it was first reported by Ingham and Kelmanson[10] and subsequently verified by Georgiou *et al.*[11] and Tanner and Huang.[12] Trogdon and Joseph[13] extended the Wiener–Hopf method to the calculation of the axisymmetric version of the stick-slip problem. The local analysis near the singularity at the lip was performed even earlier by Michael[14] and Moffatt[15] since it is a special case of the flow of a viscous fluid near a corner of an arbitrary angle formed by a solid wall and a flat free surface. From the latter analysis it is derived that for a Newtonian fluid, the velocity components vary as the square root of the radial distance from the singular point, resulting in a square root singular dependence for the stresses and the pressure.

Georgiou *et al.*[11] suggested that it would be useful if one could use this knowledge about the form of the singularity around the die lip to improve the numerical solution in the neighborhood of the singularity. To this end they introduced the singular finite element method (SFEM) for the numerical simulation of the planar stick-slip problem. They showed that the convergence of the solution near the singularity could be greatly enhanced by these special elements in comparison to the ordinary Lagrangian-type finite elements. Later Salamon *et al.*[16] showed that an extremely fine mesh was indeed needed in order for the ordinary finite element method (OFEM) to resolve the flow around the singularity with the same accuracy as that achieved by SFEM with a relatively coarser mesh. Although the success of SFEM is evident, it has a significant drawback: It cannot be applied if the form of the singularity is unknown and, unfortunately, this is exactly the case when it comes to viscoelastic fluids.

Because of the profound interest on the process of viscoelastic extrusion, the simulation of the steady viscoelastic stick-slip flow has received significant attention in the past. One of the first attempts to simulate the viscoelastic stick-slip flow was made by Coleman[17] using a boundary integral solution method to simulate the flow for an Oldroyd-B fluid for Weissenberg numbers up to 2.6. Later Marchal and Crochet[18] were able to perform viscoelastic simulations for a Maxwell and an Oldroyd-B fluid up to Wi=27. In order to achieve this, they used the mixed finite element method combined with an inconsistent streamline upwind (SU) method to discretize the constitutive equation, which method, however, is recognized to be overdiffusive. Rosenberg and Keunings[19] performed simulations for an Oldroyd-B fluid using a streamline integration method achieving convergence, however, only up to fairly low Weissenberg numbers Wi=0.5. Shortly after, Owen and Phillips[20] presented simulations for an Oldroyd-B fluid using an algorithm based on a domain decomposition method in a similar range of Weissenberg numbers. The same model was also used by Salamon *et al.*[21] to study both analytically and numerically the partial-slip/slip flow. Their efforts were focused on the examination of the flow very close to the singularity. To achieve that, they used highly refined meshes around the singularity for their numerical computations, the results of which showed remarkable agreement with their analytical calculations. Later on, Fortin *et al.*[22] and Baaijens[23] presented numerical experiments for two low-order discontinuous Galerkin methods for the stick-slip flow of a linear PTT fluid reaching very high values of Wi (for large values of the elongational parameter ε no upper limit was found). Finally, quite recently Ngamaramvaranggul and Webster[24] used the semi-implicit Taylor–Galerkin/pressure-correction method to perform time dependent simulations for the stick-slip problem of an Oldroyd-B fluid until it reached steady state. Convergence up to Wi=2.2 was achieved.

Apparently, the stick-slip flow of a PTT fluid has been addressed only in a slit die by Fortin *et al.*[22] and Baaijens,[23] although with a numerical method that does not generate the global Jacobian matrix of the problem. On the other hand, examination of the linear stability of this flow requires this Jacobian matrix in order to compute its eigenvalues and eigenvectors. This led us to decide to apply a different solution method to the stick-slip problem of the PTT fluid model than those already presented and examine both the slit and the cylindrical dies. Hence, the main objective of this paper is to develop this accurate and efficient numerical method in order to solve the steady viscoelastic two-dimensional and axisymmetric stick-slip flow, to demonstrate that our results converge with mesh refinement and that the computed variables are integrable even near the singularity. Moreover we have the opportunity to examine in detail the form of the solution very close to the die exit. This is important since it has been proven impossible to date to derive an analytical solution for a viscoelastic fluid. Then the stability of such steady state solutions can be examined.

The rest of this paper is organized as follows. We briefly present the governing equations and the boundary conditions for this problem in Sec. II, and the numerical algorithm, used in our calculations, in Sec. III. In Sec. IV, we examine the accuracy of our results by comparing them to existing ones, especially for Newtonian fluids, and the convergence and integrability of all variables, especially near the singularity and, finally, present a parametric study of the steady state solution. Conclusions are drawn in Sec. V.

II. PROBLEM FORMULATION

The steady, planar, and axisymmetric stick-slip flow of a viscoelastic fluid is examined. The fluid is assumed to be incompressible with constant density ρ, relaxation time λ, and total zero-shear viscosity $\mu=\mu_s+\mu_p$, where μ_s and μ_p are the solvent and polymer contributions, respectively. Figure 1 shows the geometry of this problem and its dimensions. The viscoelastic fluid initially flows inside the die of diam-

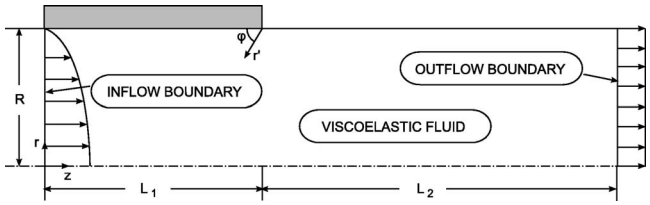

FIG. 1. Schematic of the flow geometry and coordinate system.

eter or width $2R$ and length L_1. The velocity and pressure fields rearrange as the fluid exits the die until far from it, at distance L_2 from the exit, a fully developed shear-free flow is obtained.

All lengths are scaled with the half of the die gap, R, and velocities with the mean velocity at the inflow boundary, V, while both the pressure and stress components are scaled with a viscous scale, $\mu V/R$. Thus, the dimensionless groups that arise are the Reynolds number, $\mathrm{Re}=\rho VR/\mu$, which hereafter is set to zero under the creeping flow assumption, the Weissenberg number, $\mathrm{Wi}=\lambda V/R$, the ratio of the Newtonian solvent viscosity over the total viscosity, $\beta=\mu_s/\mu$, and the geometric ratios $l_1=L_1/R$ and $l_2=L_2/R$.

Inserting the previously defined characteristic quantities into the momentum and mass conservation equations, we obtain

$$\underline{\nabla} P - \underline{\nabla} \cdot \underline{\underline{\tau}} = 0, \tag{1}$$

$$\underline{\nabla} \cdot \underline{v} = 0, \tag{2}$$

where $\underline{\nabla}$ denotes the gradient operator for either the planar or the cylindrical coordinates, $\underline{v}$ and P are the velocity vector and pressure fields, respectively, and $\underline{\underline{\tau}}$ is the extra stress tensor, which is split into a purely viscous part, $2\beta\underline{\underline{\dot{\gamma}}}$ and a polymeric contribution $\underline{\underline{\tau}}_p$,

$$\underline{\underline{\tau}} = 2\beta\underline{\underline{\dot{\gamma}}} + \underline{\underline{\tau}}_p, \tag{3}$$

where $\underline{\underline{\dot{\gamma}}}$ is the rate of strain tensor defined as $\underline{\underline{\dot{\gamma}}}=\frac{1}{2}(\underline{\nabla}\underline{v}+\underline{\nabla}\underline{v}^T)$.

To complete the description, a constitutive equation that describes the rheology of the fluid is required in order to determine the viscoelastic part of the extra stress tensor. As such, we use the following differential model that has been proposed by Phan-Thien and Tanner:[5]

$$Y(\underline{\underline{\tau}}_p)\underline{\underline{\tau}}_p + \mathrm{Wi}\ \overset{\square}{\underline{\underline{\tau}}}_p - 2(1-\beta)\underline{\underline{\dot{\gamma}}} = 0 \tag{4}$$

where the symbol $\square$ over the viscoelastic stress denotes the Gordon–Schowalter derivative defined as

$$\overset{\square}{\underline{\underline{X}}} = \frac{D\underline{\underline{X}}}{Dt} - (\underline{\nabla}\underline{v} - \xi_s\underline{\underline{\dot{\gamma}}})^T \cdot \underline{\underline{X}} - \underline{\underline{X}} \cdot (\underline{\nabla}\underline{v} - \xi_s\underline{\underline{\dot{\gamma}}}). \tag{5}$$

Two forms of the PTT model are in common use, namely, the linearized form,[5] where the function $Y(\underline{\underline{\tau}}_p)$ is

$$Y(\underline{\underline{\tau}}_p) = 1 + \frac{\varepsilon}{1-\beta}\mathrm{Wi}\ tr\underline{\underline{\tau}}_p \tag{6a}$$

and the exponential form[6] with

$$Y(\underline{\underline{\tau}}_p) = \exp\left[\frac{\varepsilon}{1-\beta}\mathrm{Wi}\ tr\underline{\underline{\tau}}_p\right]. \tag{6b}$$

In our simulations, primarily we have used the exponential form of the PTT model and assumed no slip between the polymeric chains and the continuous medium (assumption of affine motion), $\xi_s=0$. By setting ξ_s equal to zero the Gordon–Schowalter derivative reduces to the upper convective one. The only other parameter of the PTT model, ε, imposes an upper limit to the elongational viscosity, which decreases as this parameter increases. Moreover, increasing ε increases the shear-thinning behavior of the model. Clearly the PTT model reduces to the Oldroyd-B one by setting $\varepsilon=0$ and to the upper convected Maxwell (UCM) model by setting $\beta=0$ as well.

In order to solve accurately and efficiently various viscoelastic flows, Rajagopalan *et al.*[25] introduced the elastic-viscous split stress (EVSS) formulation. This method consists of splitting the polymeric part of the extra stress tensor into a purely elastic and a viscous part,

$$\underline{\underline{\tau}}_p = \underline{\underline{\Sigma}} + 2(1-\beta)\underline{\underline{\dot{\gamma}}}. \tag{7}$$

The success of this scheme resides on the fact that the elliptic nature of the momentum equations is ensured even for $\beta=0$. Brown *et al.*[26] proposed a modification of this model (EVSS-G) according to which an independent interpolation of the components of the velocity gradient tensor is introduced in order to satisfy the compatibility in the approximation between elastic stress and velocity gradients in the constitutive equation. The corresponding equation that must be solved is

$$\underline{\underline{G}} = \underline{\nabla}\underline{v}. \tag{8}$$

Thus after reformulating the momentum and constitutive equations using the EVSS-G formulation we obtain

$$\underline{\nabla} P - \underline{\nabla} \cdot \underline{\underline{\Sigma}} - 2\underline{\nabla} \cdot \underline{\underline{\dot{\gamma}}} = 0, \tag{9}$$

$$Y(\underline{\underline{\tau}}_p)\underline{\underline{\Sigma}} + \mathrm{Wi}\ \overset{\square}{\underline{\underline{\Sigma}}} + 2\ \mathrm{Wi}(1-\beta)\overset{\square}{\underline{\underline{D}}} - 2(1-\beta)[1-Y(\underline{\underline{\tau}}_p)]\underline{\underline{D}} = 0, \tag{10}$$

where $\underline{\underline{D}}=\frac{1}{2}(\underline{\underline{G}}+\underline{\underline{G}}^T)$. Moreover the definition of the Gordon–Schowalter derivative becomes

$$\overset{\square}{\underline{\underline{X}}} = \frac{D\underline{\underline{X}}}{Dt} - \underline{\underline{G}}^T \cdot \underline{\underline{X}} - \underline{\underline{X}} \cdot \underline{\underline{G}}. \tag{11}$$

Along the free (slip) surface of the fluid ($r=1$ and $l_1 \le z \le l_2$) we impose the kinematic equation which for the stick-slip problem reduces to

$$v_r = 0 \tag{12a}$$

and the shear-free condition on this straight surface becomes

$$\tau_{rz} = 0. \tag{12b}$$

On the die wall ($r=1$ and $0 \le z \le l_1$) we impose the usual no-slip, no-penetration conditions

$$v_z = 0, \tag{13a}$$

$$v_r = 0. \tag{13b}$$

We also have to apply boundary conditions at the entrance of the die and at the outflow boundary. We consider that both boundaries are far enough from the die exit and thus we assume that the flow in each boundary is fully developed. Therefore at the outflow boundary $(z=l_1+l_2)$ we impose a uniform velocity profile,

$$v_r = 0, \tag{14a}$$

$$\frac{\partial v_z}{\partial z} = 0. \tag{14b}$$

At the die entrance $(z=0)$, besides the boundary conditions for the velocity we also have to apply boundary conditions for the polymeric part of the stresses due to the hyperbolic character of the constitutive equation. The flow there is considered to be fully developed and therefore the velocity in the r-direction is equal to zero, $v_r=0$, while v_z as well as the stresses are functions of r. As for the pressure it can be easily shown using the r-component of the momentum equation that it varies only in the z-direction. From the z-component of the momentum equations we get

$$\frac{1}{r^j}\frac{\partial}{\partial r}(r^j \tau_{rz}) = \frac{dP}{dz}, \tag{15}$$

where the superscript j identifies the flow geometry, with $j=0$ and $j=1$ for the planar and the cylindrical case, respectively. The above equation using Eq. (3) gives

$$\frac{1}{r^j}\frac{\partial}{\partial r}\left[r^j\left(\tau_{prz} + \beta\frac{dv_z}{dr}\right)\right] = \frac{dP}{dz}. \tag{16}$$

Moreover for this kind of flow, the constitutive equation, assuming that $\xi_s=0$, reduces to

$$\tau_{prr} = \tau_{p\theta\theta} = 0, \tag{17a}$$

$$Y(\underline{\underline{\tau}}_p)\tau_{prz} = (1-\beta)\frac{dv_z}{dr}, \tag{17b}$$

$$Y(\underline{\underline{\tau}}_p)\tau_{pzz} = 2\ \mathrm{Wi}\ \tau_{prz}\frac{dv_z}{dr}. \tag{17c}$$

Equations (16), (17b), and (17c) can be solved numerically by imposing, on the die wall $(r=1)$, the no-slip condition, $v_z=0$, and on the axis or plane of symmetry $(r=0)$, the typical symmetry condition, $\partial v_z/\partial r=0$. More generally, steady state solutions of PTT fluid models driven by a pressure gradient inside ducts or by gravity over a solid surface have been presented in Refs. 27 and 28, respectively. The pressure drop, dP/dz, which appears in the above equations, is determined by demanding that the dimensionless mean velocity is equal to unity since the mean velocity at the inflow boundary, V, is used as a characteristic velocity for nondimensionalizing the governing equations. Therefore the additional equation that arises is

$$\bar{v}_z = (j+1)\int_0^1 v_z r^j dr = 1. \tag{18}$$

Finally to complete our model we have to set a datum pressure and as such, we impose a zero value to the pressure at a node of the outflow boundary $[P(r=1,z=l_1+l_2)=0]$.

III. NUMERICAL IMPLEMENTATION

In order to solve numerically the governing equations for the viscoelastic stick-slip flow, we used the mixed finite element method to discretize the velocity, pressure, and stress fields.

A. Finite element formulation

The physical domain was discretized using triangular elements. We approximate the velocity vector with six-node Lagrangian basis functions, ϕ^i, and the pressure, the elastic stresses, as well as the velocity gradients with three-node Lagrangian basis functions, ψ^i.

For the momentum and mass balances, we employ the finite element/Galerkin method, which after applying the divergence theorem results in the following weak forms:

$$\int_\Omega [-P\underline{\nabla}\phi^i + \underline{\nabla}\phi^i \cdot \underline{\underline{\Sigma}} + 2\underline{\nabla}\phi^i \cdot \underline{\underline{\dot{\gamma}}}]d\Omega - \int_\Gamma [\underline{n}\cdot(-P\underline{\underline{I}} + \underline{\underline{\tau}})]\,\phi^i d\Gamma = 0, \tag{19}$$

$$\int_\Omega \psi^j \underline{\nabla}\cdot\underline{v}\, d\Omega = 0, \tag{20}$$

where $d\Omega$ and $d\Gamma$ are the differential volume and surface area, respectively. The surface integral that appears in the momentum equation is split into five parts, each one corresponding to a boundary of the physical domain and the relevant boundary condition is applied therein.

The continuous approximation for the components of the velocity gradient tensor is written as

$$\int_\Omega (\underline{\underline{G}} - \underline{\nabla}\underline{v})\psi^j\, d\Omega = 0. \tag{21}$$

Finally the constitutive equation due to its hyperbolic character is discretized using the streamline upwind Petrov–Galerkin (SUPG) method proposed by Brooks and Hughes,[29]

$$\int_\Omega \{Y(\underline{\underline{\tau}}_p)\underline{\underline{\Sigma}} + \mathrm{Wi}\ \overset{\square}{\underline{\underline{\Sigma}}} + 2\mathrm{Wi}(1-\beta)\overset{\square}{\underline{\underline{D}}} - 2(1-\beta)[1-Y(\underline{\underline{\tau}}_p)]\underline{\underline{D}}\}\chi^i d\Omega = 0. \tag{22}$$

The new weighting function χ^i is formed from the finite element basis function for the elastic stress components as

$$\chi^i = \psi^j + \frac{h}{|\underline{v}|}\underline{v}\cdot\underline{\nabla}\psi^j, \tag{23}$$

where $|\underline{v}|$ is the magnitude of the mean velocity and h is a characteristic length at the particular element. The mean ve-

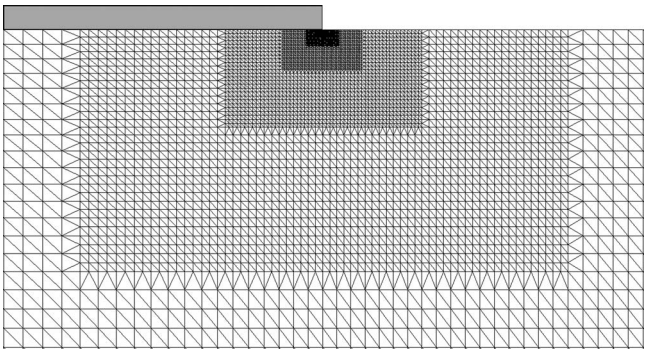

FIG. 2. Typical mesh (M10, see Table I). For clarity we show only a region around the die lip ($|z-z_c| \leq 0.04$ and $|r-r_c| \leq 0.04$) which includes the third to eighth levels of local refinement.

locity $|\underline{v}|$ in an element is defined as $|\underline{v}| = \frac{1}{3}\Sigma_{n=1}^{3}|\underline{v}|_n$, with $|\underline{v}|_n$ denoting the magnitude of the velocity at the vertices of the corresponding triangular element. As a characteristic length, h, we used the square root of the area of each triangular element.

The SFEM generally produces more accurate results near the singular point. For this reason we decided to use it also to examine the accuracy of our predictions for the simulation of the Newtonian stick-slip flow in both planar and cylindrical geometries. In this case, singular elements are only used around the die lip while the rest of the domain is discretized with ordinary elements as described above. The details of this method can be found in Refs. 11 and 30.

B. Mesh generation

A blow up of the mesh, which was used for these calculations, around the die lip only ($|z-z_c| \leq 0.04$ and $|r-r_c| \leq 0.04$, where r_c and z_c are the coordinates of the triple contact point) is presented in Fig. 2. We should note here that special care was taken for the mesh near the plane of the die exit since the flow rearrangement mostly takes place in that area, as well as near the die wall and even more so around the die lip where steep pressure or stress gradients or boundary layers may arise. Therefore, in order to resolve adequately the flow, a more refined mesh around these regions is needed. To this end, we have used a grid for the physical domain the mesh lines of which are clustered near those regions combined with a local refinement scheme using the h-method. The details of the implementation of the h-refinement method can be found in Ref. 31, whereas the clustering was performed following simple algebraic relations, as in Ref. 32.

In particular, for this problem, if we denote with η and ξ the node coordinates of a uniform mesh, the new transformed-clustered mesh would be given by the following equations in the r-direction:

$$r = \frac{k_1\left[\left(\frac{k_1+1}{k_1-1}\right)^{\eta} - 1\right]}{\left(\frac{k_1+1}{k_1-1}\right)^{\eta} + 1}. \tag{24}$$

Similarly, in the z-direction and for $0 \leq z \leq l_1$, we apply

$$z = l_1 - l_1 \frac{(k_2+1) - (k_2-1)\left(\frac{k_2+1}{k_2-1}\right)^{\omega_1}}{\left(\frac{k_2+1}{k_2-1}\right)^{\omega_1} + 1}, \tag{25a}$$

where

$$\omega_1 = 1 - \frac{l_1 - \xi}{l_1}, \tag{25b}$$

whereas for $l_1 \leq z \leq l_1 + l_2$, we use

$$z = l_1 + l_2 \frac{(k_3+1) - (k_3-1)\left(\frac{k_3+1}{k_3-1}\right)^{\omega_2}}{\left(\frac{k_3+1}{k_3-1}\right)^{\omega_2} + 1}, \tag{26a}$$

where

$$\omega_2 = 1 - \frac{\xi - l_1}{l_2}. \tag{26b}$$

The degree of refinement near the die wall is controlled by k_1, a typical value of which is 1.1. Correspondingly, parameters k_2 and k_3 are also used for controlling the degree of the refinement near the die exit in the z-direction. A typical value for both parameters and for $l_1=10$ and $l_2=50$ is 1.01. These parameter values allow for a very gradual increase in the element size away from the singularity.

Georgiou *et al.*[11] suggested that the type of triangulation could affect the performance of the SFEM and this fact motivated us to examine whether our calculations are affected in any way by the type of mesh around the singular point. To this end, we used two different types of mesh, changing each time the triangulation of the rectangular elements at the singularity. The direction of triangulation changes at the die and as a result, four triangular elements share one of their nodes at the singular point. Another possibility, which has been used quite often even in similar problems, is for the triangulation to remain unchanged inside and outside the die. In this way, only three elements share their nodes at the die lip. From our numerical experiments it was found that the former gave slightly more accurate results for the expansion coefficients of v_z near the singularity and therefore, it was used in the rest of the present work. This same mesh performs much better than the mesh with the same orientation in the triangulation in the entire domain, if extrudate swell is allowed, because the shape of the triangular element at the die lip does not get significantly distorted, even for very large deformations of the extrudate, permitting calculations up to very high Weissenberg numbers.[33] The details on the mesh used with the SFEM method can be found in Ref. 30.

In order to check the convergence of the numerical algorithm for the viscoelastic problem, we performed an extended mesh refinement study. Some useful data about the meshes that were used are presented in Table I. It is noteworthy that in meshes M1 and M2 the refinement is done only by clustering the mesh lines near the die lip, whereas meshes M3–M11 have up to ten levels of local refinement resulting in sizes of elements in M11 as small as 7×10^{-6} near the

TABLE I. Properties of typical finite element meshes used in the present work.

Mesh	No. of initial 1D Elements in the (r,z) direction	No. of refinement levels	No. of triangular elements	No. of unknowns	l_1	l_2	$\Delta r_{\min}$	$\Delta z_{\min}$
D1	(22,300)	0	13 200	123 320	15	60	1.4×10^{-2}	1.3×10^{-2}
M1	(22,240)	0	10 560	98 720	10	50	1.4×10^{-2}	1.3×10^{-2}
M2	(40,440)	0	35 200	323 532	10	50	7.2×10^{-3}	7.3×10^{-3}
M3	(40,440)	1	38 918	357 260	10	50	3.6×10^{-3}	3.6×10^{-3}
M4	(40,440)	2	44 016	403 450	10	50	1.8×10^{-3}	1.8×10^{-3}
M5	(40,440)	3	46 776	428 500	10	50	9×10^{-4}	9×10^{-4}
M6	(40,440)	4	48 077	440 356	10	50	4.5×10^{-4}	4.5×10^{-4}
M7	(40,440)	5	49 573	453 974	10	50	2.2×10^{-4}	2.2×10^{-4}
M8	(40,440)	6	50 581	463 172	10	50	1.1×10^{-4}	1.1×10^{-4}
M9	(40,440)	7	51 197	468 814	10	50	5.5×10^{-5}	5.5×10^{-5}
M10	(40,440)	8	51 517	471 764	10	50	2.8×10^{-5}	2.8×10^{-5}
M11	(40,440)	10	52 095	477 364	10	50	7×10^{-6}	7×10^{-6}

singularity. Finally, the only difference between the M1 and D1 meshes is the increase in the length inside and outside the die of D1, increasing at the same time the number of elements in the z-direction in order to retain the same degree of discretization. The resulting minimum size of elements at the singular point as well as their maximum size far from it remains the same in both M1 and D1. Calculations using either one of these two meshes produced the same results verifying that the inflow and outflow boundary conditions do not affect the solution in any way.

C. Numerical solution

The resulting set of algebraic equations for the base state problem is solved simultaneously for all variables using the Newton–Raphson method. In this way the global Jacobian matrix of the problem is generated which can be used in order to compute its eigenvalues and eigenvectors and study the stability of the stick-slip flow. The Jacobian matrix that results after each Newton iteration is stored in compressed sparse row format and the linearized system is solved by Gaussian elimination using PARDISO, a robust, direct, sparse-matrix solver, Refs. 34 and 35. The iterations of the Newton–Raphson method are terminated using a tolerance for the absolute error of the residual vector, which is set at 10^{-9}. The code was written in FORTRAN 90 and was run on a workstation with dual Dual Core Xeon CPU at 2.8 GHz in the Laboratory of Computational Fluid Dynamics. Each calculation for the steady state problem for a wide range of Weissenberg numbers typically required 2–5 days to complete depending on the mesh used.

IV. RESULTS AND DISCUSSION

In order to validate our code and verify the accuracy of our results, we will first compare them to the existing ones for the Newtonian and PTT fluids. In addition, we will demonstrate that our viscoelastic results converge with mesh refinement and proceed with the examination of the flow near the singularity. Subsequently, we will present a parametric study of our steady state calculations.

A. Comparison with previous studies

First, we solved the stick-slip flow of a Newtonian fluid using both the OFEM, which we also used for all our viscoelastic simulations, and the SFEM. In this way, we will gain valuable insight as to how the steady flow is affected by either the numerical method or the form of the mesh around the singularity before proceeding with the viscoelastic calculations and their stability.

The flow field of a Newtonian fluid is well known for this problem and will not be reproduced in this paper, but can be found in Ref. 30. For a Newtonian fluid the local asymptotic analysis[15] around the singularity for the planar problem shows that the form of the z-component of the velocity along the free surface is given by

$$v_z = 2a_{1/2}z^{1/2} - 2a_{3/2}z^{3/2} + 2a_{5/2}z^{5/2} + O(z^{7/2}). \tag{27}$$

This equation was used to fit our finite element results for the z-component of the velocity near the die edge (in the interval $l_1 \le z \le l_1+1$) and the computed values for the coefficients are presented in Table II along with those obtained by several previous analytical or numerical studies. We can see clearly that the computed values for the planar case are in very good agreement with the earlier ones. Moreover, we observe that the SFEM gives accurate results even with a coarser mesh as was already noted by Georgiou *et al.*[11] To achieve the same accuracy using the OFEM, one would have to use an extremely refined mesh around the singularity as was shown by Salamon *et al.*[16] Indeed using our finest mesh (M11), we were able to calculate the corresponding coefficients with high accuracy. The best method available for a Newtonian fluid in a planar geometry is the singular function boundary element method developed by Elliotis *et al.*[36] The success of this method comes from the fact that it calculates directly the singular coefficients. In fact, the first coefficient agrees to the sixth decimal digit with the analytically calculated one in Ref. 12 and, in addition, it calculates the next three coefficients converged to the fifth decimal digit. These cannot be obtained analytically.

Furthermore, Trogdon and Joseph[13] noted that the same local dependence of v_z holds for the cylindrical case since

TABLE II. Computed with meshes M2 (modified to include singular elements for SFEM) and M11 (for OFEM) expansion coefficients near the singularity for the Newtonian stick-slip flow compared to previous works.

Publication	$a_{1/2}$	$a_{3/2}$	$a_{5/2}$
	Planar die		
Present work (OFEM)	0.691 57	0.271 97	0.052 47
Present work (SFEM)	0.691 83	0.272 90	0.053 18
Georgiou *et al.*[a] (OFEM)	0.671 70	0.198 12	−0.022 97
Georgiou *et al.*[a] (SFEM)	0.691 73	0.271 68	0.050 13
Salamon *et al.*[b]	0.691 60	0.271 83	0.052 32
Ingham and Kelmanson[c]	0.691 08	0.264 35	0.049 62
Richardson[d]	0.581 00	⋯	⋯
Tanner and Huang[e]	0.690 99	⋯	⋯
Elliotis *et al.*[f]	0.690 99	0.264 50	0.030 37
	Cylindrical die		
Present work (OFEM)	0.797 26	0.434 16	0.123 73
Present work (SFEM)	0.796 78	0.432 38	0.122 31
Tanner and Huang[e]	0.651 47	⋯	⋯

[a]Reference 11.
[b]Reference 16.
[c]Reference 10.
[d]Reference 9.
[e]Reference 12.
[f]Reference 36.

this geometry is locally, at the die lip, similar to the planar one. Hence the same equation was used to fit the z-component of the velocity in the cylindrical geometry. The resulting coefficients are given in the same table. The computed values using the SFEM as well as the OFEM method are in good agreement. These results, however, differ significantly from the value of $a_{1/2}$ that was given earlier by Tanner and Huang.[12] They used the same J-integral to calculate the coefficient in both the planar and axisymmetric cases. We can see in Table II that indeed, in planar flow their computed value is highly accurate. On the other hand, their computed value for the axisymmetric case is inaccurate. This is because the J-integral cannot be used without modification for the axisymmetric flow since in this case it is not path independent any more. To get a path-independent form one has to add to the J-integral an additional surface integral and should choose a path that does not intersect the axis of symmetry.[37] This makes the computation nontrivial and we did not pursue it since it would be beyond the scope of this paper. Finally, we compared the semianalytical solutions given by Trogdon and Joseph[13] to our numerical ones. Using the software "DATA THIEF" we replotted variables given in this paper, including the singular pressure, and observed that they are virtually indistinguishable from ours in all cases so they will not be reproduced herein.

From the local asymptotic analysis for Newtonian stick-slip flow we know that the pressure is singular for both geometries with a characteristic square root singularity at the die lip. Figure 3 depicts the dependence of the pressure along the free surface of the extrudate on the distance from the singularity. It is clear that the predicted value for the slope of the pressure is very close to −0.5 as predicted by theory and is in good agreement with the values given by Salamon *et al.*[16] for the planar case. Again we observe that very close

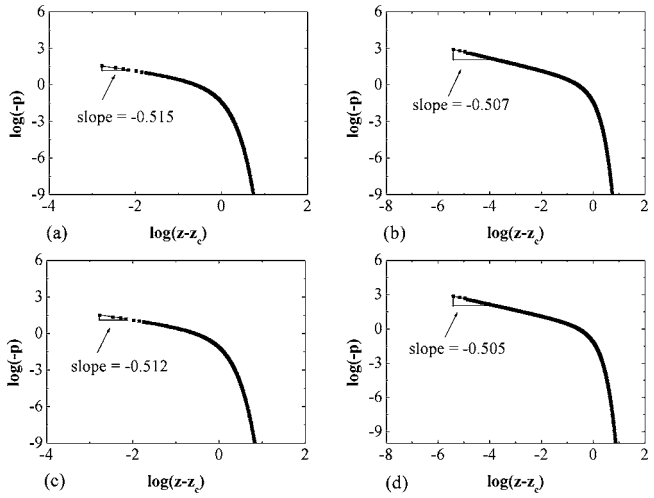

FIG. 3. Dependence of $\log(-p)$ on $\log(z-z_c)$ along the free surface of the fluid for a cylindrical die using the (a) SFEM and (b) OFEM and for a planar die using the (c) SFEM and (d) OFEM. Mesh M11 is used for the OFEM calculations and a modification of the M2 mesh for the SFEM calculations.

to the singularity, the SFEM gives slightly less accurate values using a significantly coarser mesh than the OFEM. This should be anticipated since SFEM inherently takes into consideration the known form of the singularity for the Newtonian fluids. Nevertheless, this is also its main drawback since for an unknown form of singularity, which is the case for a viscoelastic fluid, the SFEM cannot be used.

In order to verify the accuracy of our code for the case of a viscoelastic fluid, we also performed a comparison with the results of the simulations reported by Baaijens[23] for the stick-slip flow using the linear affine PTT model. This author used the discontinuous Galerkin method with constant stress elements for his calculations. As a typical comparison, we present in Fig. 4 the first normal stress difference along the die wall and the slip surface ($r=1$) also using the linear PTT model for Wi=19, $\beta=0$, and for two different values of the elongation parameter, ε. This value of Wi corresponds to De=88.83 according to the definition of Baaijens.[23] We

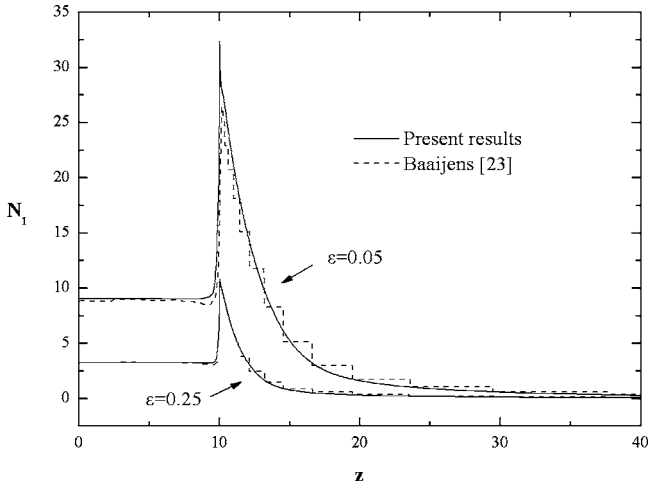

FIG. 4. Comparison of the predictions for N_1 for Wi=19, $\beta=0$, $l_1=10$, and $l_2=50$ and for two different values of ε with results given by Baaijens (Ref. 23). Mesh M1 is used.

TABLE III. Exit pressure losses, ex, axial velocity v_z, pressure P, and stresses Σ_{rr}, Σ_{rz}, Σ_{zz}, and $\Sigma_{\theta\theta}$ at the position $(r,z)=(0.923,10)$, which is fairly close to the singular point computed with various meshes for Wi=2, $\varepsilon=0.02$, $\beta=0$, $l_1=10$, and $l_2=50$.

Mesh	ex	v_z	P	Σ_{rr}	Σ_{rz}	Σ_{zz}	$\Sigma_{\theta\theta}$
			Cylindrical die				
M1	2.250	0.5233	10.070	0.7973	4.1710	17.001	−0.1273
M2	2.257	0.5195	10.175	0.7958	4.1760	17.131	−0.1277
M3	2.259	0.5180	10.220	0.7882	4.2135	17.260	−0.1278
M4	2.262	0.5169	10.265	0.7871	4.2127	17.338	−0.1269
M5	2.263	0.5163	10.288	0.7887	4.2081	17.384	−0.1263
M6	2.264	0.5160	10.298	0.7892	4.2066	17.395	−0.1261
Richardson extrapolation	2.264	0.5159	10.300	0.7893	4.2063	17.397	−0.1260
			Planar die				
M1	1.344	0.4355	5.466	0.6362	3.4191	14.335	⋯
M2	1.346	0.4317	5.537	0.6367	3.4229	14.416	⋯
M3	1.348	0.4301	5.582	0.6321	3.4422	14.544	⋯
M4	1.349	0.4293	5.605	0.6306	3.4395	14.588	⋯
M5	1.350	0.4289	5.617	0.6310	3.4363	14.612	⋯
M6	1.350	0.4287	5.622	0.6314	3.4354	14.622	⋯
Richardson extrapolation	1.350	0.4287	5.623	0.6315	3.4352	14.624	⋯

should note here that the use of constant stress elements by Baaijens[23] resulted in piecewise constant curves for the first normal stress difference. This unsmooth solution for the stresses is inappropriate for studying its stability. Moreover, Fig. 13 in his paper could not be read very well near the singularity for the case of $\varepsilon=0.25$ and it appears in Fig. 4 with a gap in that region. Despite this fact, it is clear that the results of our computations are in very good agreement with the ones given by Baaijens.[23]

B. Convergence with mesh refinement

The convergence of the finite element calculations with mesh refinement is shown in Table III. It compares, for six different meshes at a given point very close to the singularity, the values of the z-component of the velocity vector, pressure, elastic stresses, and exit pressure losses, ex, which is defined as

$$\mathrm{ex} = \frac{\Delta P - \Delta P_o}{2\tau_w}, \tag{28}$$

where ΔP is the total pressure drop between the inlet and the outlet in the stick-slip flow, whereas ΔP_o is the pressure drop for fully developed flow inside a die of the same length and τ_w is the corresponding shear stress at the die wall at the inflow boundary. In addition, we have performed a Richardson extrapolation of our predictions and the computed values are also presented in this table. The extrapolation was done considering the series of the computed values of each variable for the different meshes at the given point, shown in the table. As a characteristic length we used the minimum element size of each mesh in the radial direction. We can see that all variables converge with mesh refinement.

To quantify the error and its dependence on the mesh, we prepared Fig. 5 for a cylindrical die. The rate of convergence is evaluated by computing the Euclidean norm of the differences in the values obtained with any mesh, Mi (i=2,3,4,5), to those obtained by the finest mesh (M6) for the same variables. This Euclidean norm includes only un-

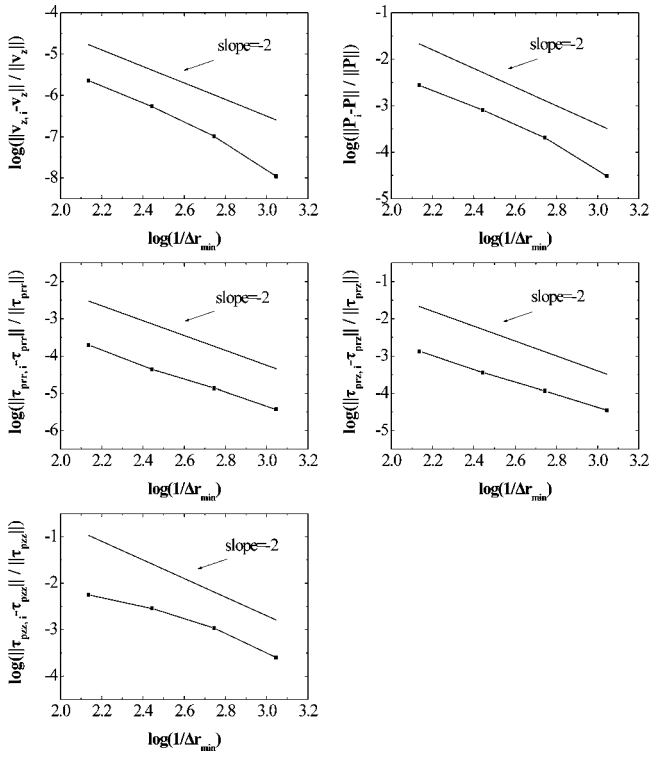

FIG. 5. The relative error of the axial velocity, pressure, and stresses at the exit of a cylindrical die ($z=10$) for Wi=2, $\varepsilon=0.02$, $\beta=0$, $l_1=10$, $l_2=50$, and various meshes. As a reference value the solution with mesh M6 is used, while the vectors $v_{z,i}$, P_i, $\Sigma_{rr,i}$, $\Sigma_{rz,i}$, and $\Sigma_{zz,i}$ are calculated using meshes M2–M5.

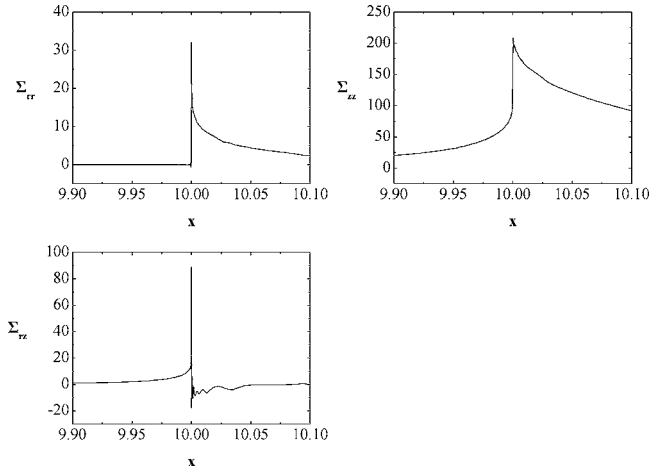

FIG. 6. Local behavior of Σ_{rr}, Σ_{rz}, and Σ_{rz} for Wi=0.5, ε=0.02, β=0, l_1=10, and l_2=50 with mesh M10. Planar die.

knowns from the cross section at the die exit ($0 \le r \le 1$, $z=l_1$) where the effects of the singularity are expected to be most apparent. For the computation of the norms, the values of all variables at meshes other than the coarsest one were interpolated at the locations corresponding to the coarsest mesh. Clearly for all the variables the relative error decreases quadratically with mesh refinement. We have also computed similar norms along the free surface near the die exit ($r=1$, $l_1 \le z \le l_1+1$) and the convergence rate was found to be the same. The convergence is similar for the case of a planar die.

C. Form of the singularity for a viscoelastic fluid

Having confirmed that our computations for the viscoelastic fluid converge with mesh refinement, we proceed with the investigation of the form of the singularity for the case of a PTT fluid. Of course it is expected that the form of the singularity will not be the same as in the Newtonian case. When it comes to the viscoelastic stick-slip flow, this singularity may lead to major numerical difficulties or even to numerical results with no physical meaning, when the elastic stresses predicted by the corresponding viscoelastic model are not integrable near the die lip. This fact motivated several researchers in the past to examine carefully the flow for various viscoelastic fluid models near such singularities, which appear in general near re-entrant corners.[12,38–42] We believe that it would be very useful to compare the results of our computations with the findings of the aforementioned works. Moreover, since the analytical calculations have been proven quite difficult for viscoelastic fluids, our results could elucidate the form of the solution near the singularity.

To start with, Fig. 6 depicts the variation of the elastic stresses for the case of a planar die, very close to its exit along $r=1$ in the range $9.9 \le z \le 10.1$ for Wi=0.5, ε=0.02, β=0, l_1=10, and l_2=50. It is evident from the plots that all the stresses become singular as the die lip is approached. The solution for Σ_{rr} and Σ_{zz} is very smooth even close to the die exit whereas for Σ_{rz} some oscillations arise. Salamon *et al.*[21] studied the partial-slip/slip flow for an Oldroyd-B fluid and have shown both numerically and analytically that Σ_{rr} and

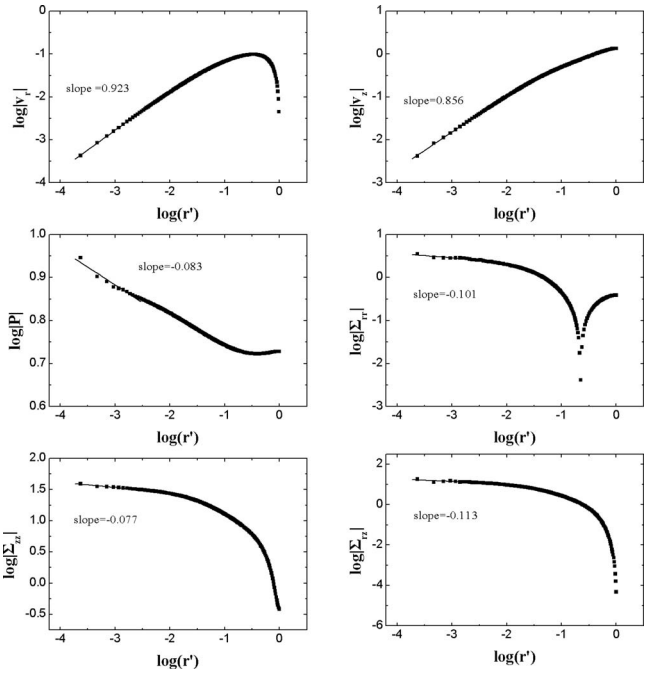

FIG. 7. Asymptotic behavior near the singularity for the velocities, pressure, and elastic stresses at the die exit ($z=10$) for Wi=2, ε=0.02, β=0, l_1=10, and l_2=50 with mesh M6. Planar die.

Σ_{zz} are singular, whereas Σ_{rz} exhibit a distinct jump at the die exit. The nonsingular behavior in this case is attributed to the presence of partial slip along the wall. On the other hand, in our case there is no slip at the die wall and as a result Σ_{rz} becomes singular close to the die lip.

It is expected that the variation of the velocities, pressure, and stresses depends both on the radial distance, r', from the singularity as well as on the corresponding angle, ϕ (see Fig. 1 for their definitions). To start with, the dependence of the velocities, pressure, and elastic stresses on the distance from the die lip at $z=10$ ($\phi=90°$) is presented in Fig. 7 for the case of a planar die and for Wi=2, ε=0.02, β=0, l_1=10, and l_2=50. The slopes that are presented in this figure were calculated performing a linear fit for all the variables using their computed values at the ten closest nodes to the die lip. We observe that for the PTT fluid the slopes for both velocity components have increased significantly compared to the value of 0.5 which is predicted theoretically for a Newtonian fluid. Therefore it can be deduced that the corresponding velocity gradients are less singular than in the Newtonian case. The same holds for the pressure as well as the polymeric part of the stresses as can be seen in the figure. This finding is in accordance with the works of Renardy[39] and of Evans and Sibley[41,42] who showed analytically, assuming a Newtonian velocity field, that the elastic stresses for a PTT fluid near a re-entrant corner are less singular than the Newtonian stresses. On the other hand, Hinch[40] and Renardy[38] showed that for an Oldroyd-B and a UCM fluid, respectively, the predicted singularity is more intense than for a Newtonian fluid. Even so, the computed stresses were found to be integrable near the singularity in contrast to the case of the second order fluid which was shown by Tanner and Huang[12] to predict nonintegrable stresses near a re-

TABLE IV. Convergence of computed slopes for the asymptotic behavior near the singularity for the velocities, pressure, and elastic stresses at $z=10$ ($\phi=90°$) and for various values of Wi, $\varepsilon=0.02$, and $\beta=0$. Planar die and ePTT fluid model.

Slope of…	v_r	v_z	P	Σ_{rr}	Σ_{rz}	Σ_{zz}
			Wi=0.5			
M2	0.662	0.558	−0.161	−0.358	−0.512	−0.651
M3	0.706	0.581	−0.233	−0.446	−0.554	−0.626
M4	0.751	0.626	−0.278	−0.410	−0.521	−0.538
M5	0.794	0.680	−0.290	−0.336	−0.428	−0.412
M6	0.824	0.724	−0.276	−0.259	−0.327	−0.291
M7	0.859	0.770	−0.256	−0.205	−0.252	−0.208
M8	0.880	0.799	−0.233	−0.169	−0.202	−0.155
M9	0.890	0.815	−0.212	−0.148	−0.169	−0.122
M10	0.906	0.832	−0.193	−0.146	−0.148	−0.106
			Wi=2.0			
M2	0.820	0.743	−0.081	−0.324	−0.331	−0.226
M3	0.871	0.793	−0.086	−0.206	−0.225	−0.156
M4	0.896	0.823	−0.086	−0.149	−0.167	−0.115
M5	0.912	0.844	−0.085	−0.118	−0.133	−0.091
M6	0.923	0.856	−0.083	−0.101	−0.113	−0.077
			Wi=5.0			
M2	0.925	0.872	−0.052	−0.142	−0.133	−0.059
M3	0.954	0.897	−0.053	−0.079	−0.074	−0.039
M4	0.962	0.906	−0.052	−0.054	−0.051	−0.032

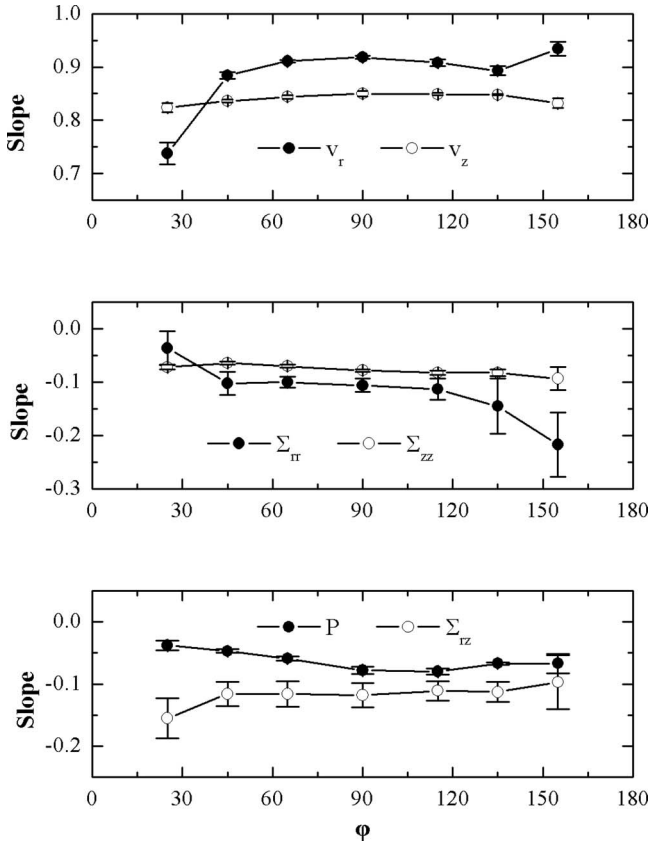

FIG. 8. Calculated slopes of the asymptotical behavior of the velocities, pressure, and elastic stresses for various angles near the singularity and for Wi=2, $\varepsilon=0.02$, and $\beta=0$ with mesh M6. Planar die.

entrant corner. We should mention that for the case of a cylindrical die the form of the singularity is expected to be the same as the planar one since the cylindrical geometry approaches a planar one when a very thin annulus is examined as the one very close to the singularity. We found that this is the case indeed, but the corresponding figures are not shown here for conciseness.

Although we have already examined the convergence of the solution with mesh refinement, it is very important to examine its convergence very close to the singularity. The reason for this is the fact that very close to the die lip high stresses arise which give rise to very thin boundary layers and thus even though the solution may converge far from the singularity, it may not have converged near it. To examine this carefully we have prepared Table IV, where we have calculated the slopes for all the variables for three different Wi numbers using various meshes. The slopes were calculated using their computed values at the ten closest nodes to the die lip for each mesh, just like in Fig. 7. The slopes presented in this table were calculated using as many refinement levels as possible to achieve convergence of the numerical scheme at a given Wi number. We notice that the maximum refinement level for which convergence of the numerical scheme can be achieved decreases with the Wi number. This is a well known problem for the numerical computation of viscoelastic flows and was also discussed in Refs. 21 and 43. Beginning with the case of the highest Wi number (Wi=5) we can see that the computed values of the slopes converge with mesh refinement even though the numerical scheme could achieve convergence only up to mesh M4. Obviously, more refinement levels are needed for the slopes to converge for Wi=2 and even more for the case of Wi=0.5. The latter could be attributed to the fact that the elongational as well as the shear viscosity of the PTT fluid increase as the Wi decreases resulting in higher stresses near the singularity (see Fig. 20 in Sec. IV D) and, consequently, the rate of convergence for Wi=0.5 is much slower than for higher values of Wi. Nevertheless, we observe that the computed values of the slopes for all variables seem to converge to the same value for all Wi numbers even though Wi was increased tenfold. This is in agreement with the findings of Salamon *et al.*[21] where it was also shown analytically as well as numerically that the solution near the singularity does not depend on Wi but viscoelasticity enters the leading order solution only through the dimensionless solvent viscosity.

Hagen and Renardy[44] performed a boundary layer analysis for the linear PTT and the Giesekus model for high Weissenberg number flows. This work is of relevance here because we expect that close to the singularity, the local Weissenberg tends to infinity since at the die lip the rate of strain becomes infinite. They studied the case of the elongational parameter, ε, being of order 1 as well as the case of very small ε. The latter is of interest here since the exponential PTT model, used herein, tends to the linear PTT model when ε is very small. Hagen and Renardy[44] suggested that the proper scaling in this case is the same as the UCM scal-

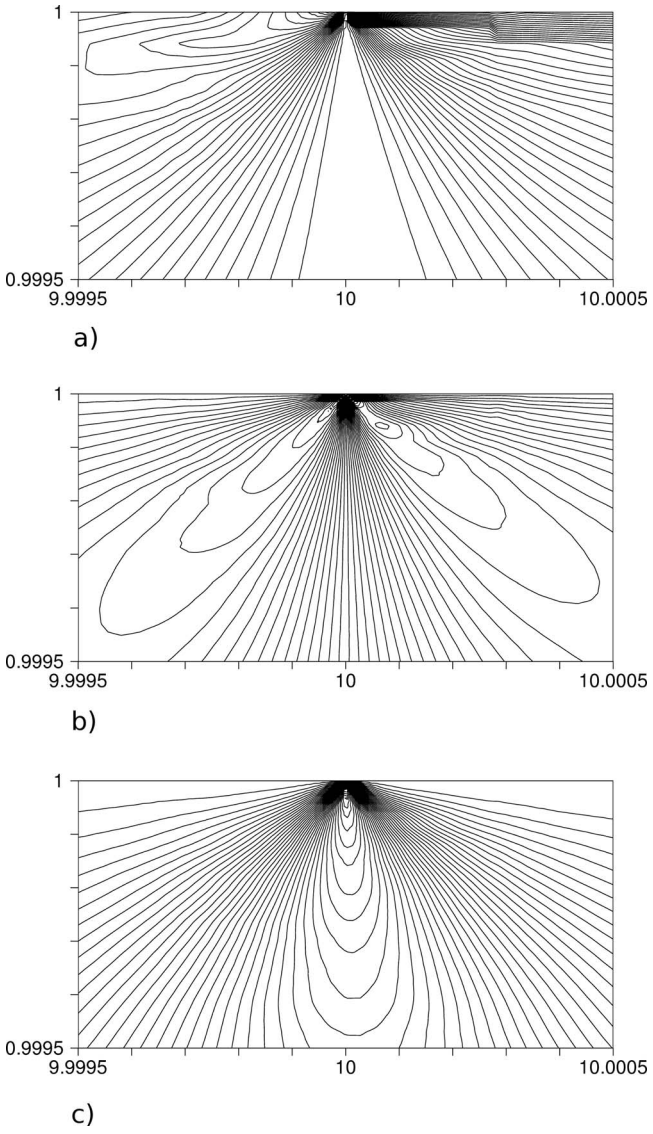

FIG. 9. Contour plots of (a) $\tau_{pr'r'}$, (b) $\tau_{pr'\phi}$, and (c), $\tau_{p\phi\phi}$ for a planar die and for Wi=0.5, ε=0.02, β=0, l_1=10, and l_2=50 using mesh M10. (The plots are restricted to $0.9995 \leq r \leq 1$ and $9.9995 \leq z \leq 10.0005$).

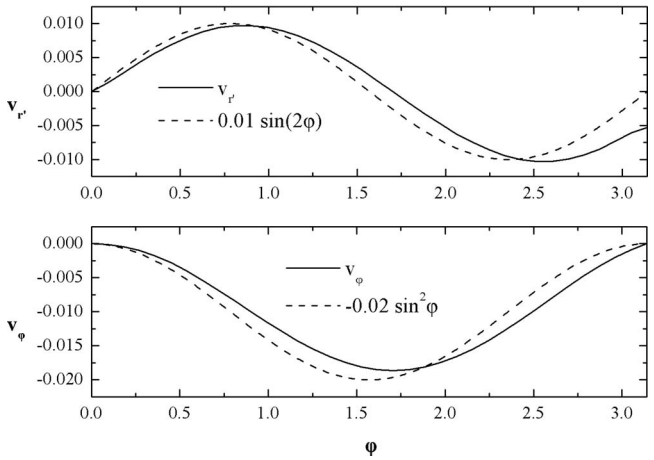

FIG. 10. Angular dependence of the velocities along the arc with r' =0.0005 for Wi=0.5, ε=0.02, β=0, l_1=10, and l_2=50 using mesh M10.

ing and they used it to rescale the equations of the linear PTT model inside the boundary layer. This scaling suggests that the thickness of the boundary layer decreases dramatically as the Wi number increases. This is in contradiction with the results shown in Table IV. In order to explain this, we should reconsider whether the UCM scaling is truly appropriate for the PTT model. In principle, it is reasonable to assume that as ε decreases, the behavior of the PTT model should tend to the UCM limit. However, even very small values of the elongational parameter change radically the properties of the fluid by introducing the effects of shear and elongational thinning, which affect significantly the stresses especially for high Wi flows. This can be seen very clearly in Figs. 19 and 20 given in Sec. IV D, where the stresses are plotted for various Wi numbers. The zz-component of stress for the UCM increases significantly with Wi whereas for the PTT fluid, all the stresses decrease with Wi. Looking more closely at the UCM scaling suggested by Hagen and Renardy,[44] we can see that the zz-component of stress should be of order Wi and the rr-component of order Wi^{-1}. These are in agreement with our findings for the UCM fluid but the former is in total disagreement with our calculations for the PTT fluid, which very clearly show that both zz and rr components of the stress decrease as Wi increases.

Now that we have confirmed that our solution converges even very close to the singularity, it would be interesting to examine the angular variation of the flow variables around the singularity. To this end we have calculated the slopes of the asymptotic behavior of the velocities, pressure, and elastic stresses for various angles near the die lip and plotted them in Fig. 8 for the case of a planar die and for Wi=2, ε=0.02, and β=0. In this figure, we also present with the error bars the standard error of the computed slope values for the linear fit of the corresponding numerical computations. The standard error of the slope is given by $\mathrm{SE}=\sqrt{[\Sigma(y_i-\hat{y}_i)^2/(N-2)]/[\Sigma(x_i-\bar{x})^2]}$, where y_i is the value of the dependent variable for the interpolation point i, $\hat{y}_i$ is the estimated value, using the computed slope, of the dependent variable for point i, x_i is the value of the independent variable for point i, $\bar{x}$ is the mean of the independent variable, and N is the number of points. We observe that the form of the solution for some of the variables varies weakly with the angle ϕ, whereas others remain almost the same for all values of ϕ. As ϕ increases, the slope of v_r increases, while the one of v_z remains almost constant. As for the elastic stresses they present different dependencies. The radial stress decreases, the shear stress increases, whereas the axial stress remains constant with ϕ. The pressure varies very little with ϕ showing the most singular behavior for ϕ=90°. Moreover, we observe that in all cases, the error of the computed slopes is minimized for ϕ=90° but increases away from this angle. Perhaps, this weak dependence of the exponent of the logarithmic singularity is the reason that a separable analytic solution near the singularity for the PTT fluid model has not been possible.

Apart from calculating the slopes at various angles it would be very interesting to examine also the form of the solution very close to the die lip. To this end, we present in

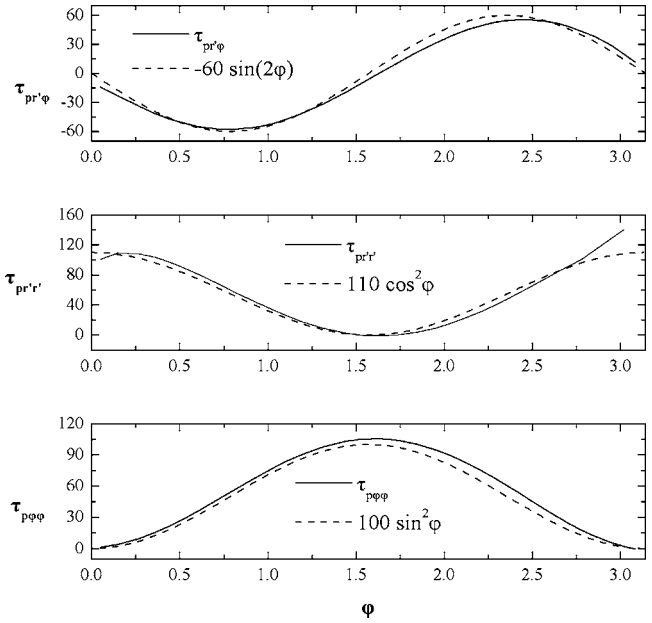

FIG. 11. Angular dependence of polymeric part of stresses along the arc with $r'=0.0005$ for Wi=0.5, $\varepsilon=0.02$, $\beta=0$, $l_1=10$, and $l_2=50$ using mesh M10.

Fig. 9 contour plots of the polymeric part of stress using cylindrical coordinates around the singularity in the ranges $0.9995 \le r \le 1$ and $9.9995 \le z \le 10.0005$. The contour lines are rather smooth verifying once more that the stresses have converged even very close to the die exit. Moreover, we observe that there is an obvious angular dependence of the stress field. This can been seen in more detail in Figs. 10 and 11 where we present the angular dependence of the velocities and the elastic stresses, respectively, at $r'=0.0005$ together with certain trigonometric functional forms. The two normal stresses are of the same magnitude but have opposite signs. The coincidence of the velocities and the stresses with the corresponding functional forms is impressive, which is another indication that the solution has converged near the singularity. In addition, we should mention that Salamon *et al.*[21] presented an analytical solution for the local asymptotic forms of the stresses near the corner for the Oldroyd-B partial-slip/slip flow. It is very interesting that in their solution $\Sigma_{r'r'}$ and $\Sigma_{\phi\phi}$ have an angular functionality of $\cos(2\phi)$ whereas $\Sigma_{r'\phi}$ has angular functionality of $\sin(2\phi)$. Even though we are studying the stick-slip flow, without the presence of any slip at the die wall and are using a different viscoelastic model, we are still getting the same form of solution for all stress components as they had.

The effect of the various rheological properties of the fluid on the form of the singularity is shown in Table V. Since, as we have seen, the slopes are calculated with smaller deviation for $\phi=90°$, we present at this position the slopes for the asymptotic behavior near the singularity for the velocities, pressure, and elastic stresses for various values of the elongational parameter, ε, and the solvent viscosity ratio, β. Varying the elongational parameter ε while keeping the rest of the parameters the same has an effect when the value of ε becomes very small. This is consistent with the analysis presented by Hagen and Renardy,[44] which suggested that the scalings inside the boundary layer should change when the elongational parameter takes very small values. As this parameter increases, the elongational as well as the shear viscosity of the fluid decreases resulting in a less singular flow field around the die lip. On the other hand, as the Newtonian solvent contribution increases, the singularity becomes intensified tending to the Newtonian limit. This is expected because then the Newtonian stresses dominate the elastic ones which are less singular near the die lip. Salamon *et al.*[21] also noticed that the partial-slip/slip flow for an Oldroyd-B fluid is dramatically different from that of a UCM fluid because of the presence of the solvent. In fact, they showed that the leading order terms in the rate of strain and elastic stress fields depend on β^{-1} increasing the strength of the singularity as β decreases. We have to keep in mind though that for an Oldroyd-B fluid, the predicted singularity is more intense than for a Newtonian fluid. Therefore in this case the addition of solvent viscosity makes the Newtonian stresses dominant over the elastic ones which are more singular and so

TABLE V. Slopes for the asymptotic behavior near the singularity for the velocities, pressure, and elastic stresses at $z=10$ ($\phi=90°$) and for various values of ε and β using mesh M6. Planar die.

Slope of…	v_r	v_z	P	Σ_{rr}	Σ_{rz}	Σ_{zz}
			Expt. PTT Wi=2.0, $\beta=0$			
$\varepsilon=0.01$	0.779	0.811	−0.039	−0.228	−0.130	−0.101
$\varepsilon=0.02$	0.923	0.856	−0.083	−0.101	−0.113	−0.077
$\varepsilon=0.05$	0.934	0.869	−0.057	−0.164	−0.109	−0.032
$\varepsilon=0.1$	0.989	0.887	−0.089	−0.122	−0.111	−0.006
			Expt. PTT $\varepsilon=0.02$, Wi=2.0			
$\beta=0$	0.923	0.856	−0.083	−0.101	−0.113	−0.077
$\beta=0.111$	0.699	0.730	⋯	−0.456	−0.261	−0.077
			Wi=2.0, $\varepsilon=0.02$, $\beta=0$			
Expt. PTT	0.923	0.856	−0.083	−0.101	−0.113	−0.077
Linear PTT	0.571	0.681	⋯	−0.165	−0.153	−0.272

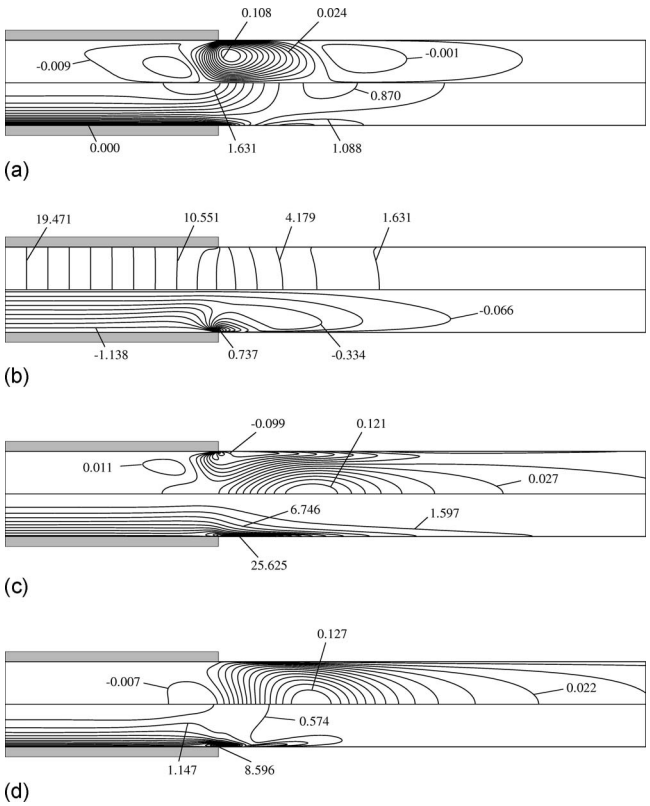

FIG. 12. Contour plots of (a) v_r, v_z, (b) P, τ_{prz}, (c) τ_{prr}, τ_{pzz}, and (d) $\tau_{p\theta\theta}$, $\dot{\gamma}$ on the upper and lower halves, respectively, for a cylindrical die and for Wi=5, $\varepsilon=0.02$, $\beta=0$, $l_1=10$, and $l_2=50$ using mesh M4 (for clarity we only show the region $5\leq z\leq 20$).

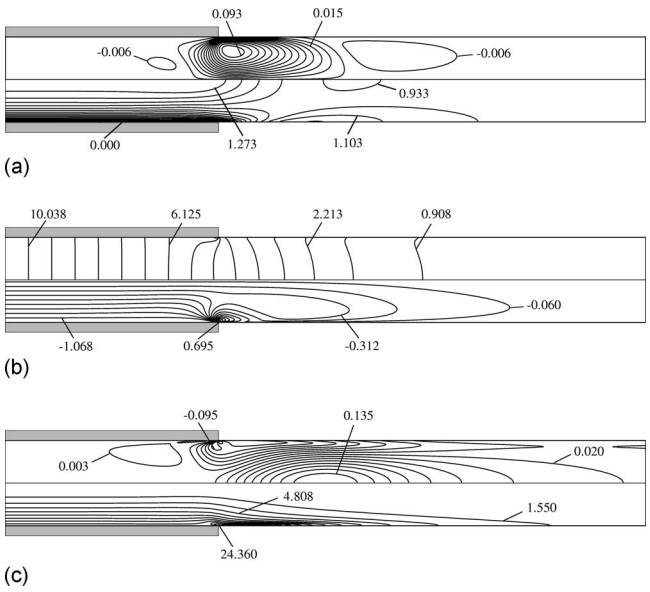

FIG. 13. Contour plots of (a) v_r, v_z, (b) P, τ_{prz}, and (c) τ_{prr}, τ_{pzz} on the upper and lower halves, respectively, for a planar die and for Wi=5, $\varepsilon=0.02$, $\beta=0$, $l_1=10$, and $l_2=50$ using mesh M4 (for clarity we only show the region $5\leq z\leq 20$).

decrease the intensity of the singularity tending to the Newtonian limit. Finally we compared the two different versions of the PTT model keeping the same values of all the parameters of the model. As we can see in the table the linear PTT model predicts a more singular flow field probably due to the fact that this model predicts a constant elongational viscosity at high elongational rates in contrast to the elongational thinning predicted by the exponential PTT model. Unfortunately, the solution for the pressure field for $\beta=0.111$ and for the case of the linear PTT model presents some oscillations very close to the singularity making it very difficult to calculate a meaningful slope and so it was preferred not to include them in this table. As a last remark it should be mentioned that for all cases, the singularity at the die exit is found to be integrable.

D. Parametric study for a viscoelastic fluid

After verifying the convergence of the computed results with mesh refinement and that the computed variables are integrable, we proceed with a parametric study of the viscoelastic stick-slip flow. The flow field for a viscoelastic fluid with Wi=5, $\varepsilon=0.02$, and $\beta=0$ is illustrated in Fig. 12 for the case of an axisymmetric die and in Fig. 13 for that of a planar die. Both figures have been obtained with the M4 mesh but the results change very little even quantitatively, at the scale of this figure had we used the M1 mesh (see also Fig. 20 in Sec. V). Once again, it is clear from the smoothness of all contour plots that all variables have converged away from the singularity. Contour plots of v_r and v_z, on the upper and lower halves, respectively, are depicted in Figs. 12(a) and 13(a). The total number of contour lines in each part of these is equal to 15. Each variable changes by the same amount between neighboring contour lines typically spanning the range between their corresponding extreme values. We observe that the velocity field differs even qualitatively from the one for a Newtonian fluid. The corresponding figures for a Newtonian fluid can be found in Ref. 30 or in Refs. 24 and 16. More specifically, the maximum values of both v_r and v_z have decreased in comparison to the corresponding Newtonian ones. This is mostly due to the shear-thinning effect which is present in PTT fluids. Shear thinning turns the Newtonian parabolic profile of v_z to a more uniform one in the r-direction, resulting in a smaller maximum at the axis of symmetry for the same average velocity. Hence, at the die exit the axial velocity component in the main flow direction has to decrease and rearrange less than its Newtonian counterpart in order to eventually approach the far field uniform flow. The local mass balance requires that the herewith generated component of v_r velocity should take (slightly) smaller values during the rearrangement of the flow field around the die exit. In spite that the fluid memory forces v_r to vary over a larger distance outside the die than in the Newtonian case, while further downstream, in a distance of about two die gaps from the die exit, v_r also changes sign and becomes negative. Clearly, elasticity causes this oscillatory variation of v_r in the z-direction and a strong radial gradient near the surface of v_r for about one die gap downstream from the die exit. This in turn, forces the axial velocity, which along the no-slip die wall was zero to not only increase abruptly outside it, at the slip surface, but also to exceed its far field value of unity. Elasticity pulls it back however, generating a local maximum in v_z along the free surface and then, it decreases monotonically toward unity.

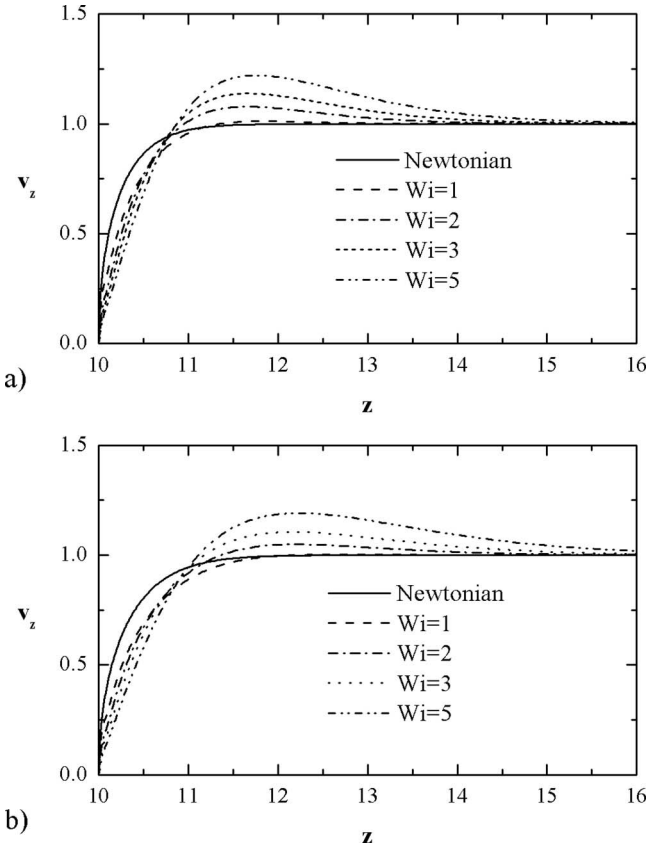

FIG. 14. Variation of the z-component of the velocity vector along the free surface ($r=1$) for $\varepsilon=0.02$, $\beta=0$, and various Wi numbers: (a) cylindrical die and (b) planar die, mesh M2.

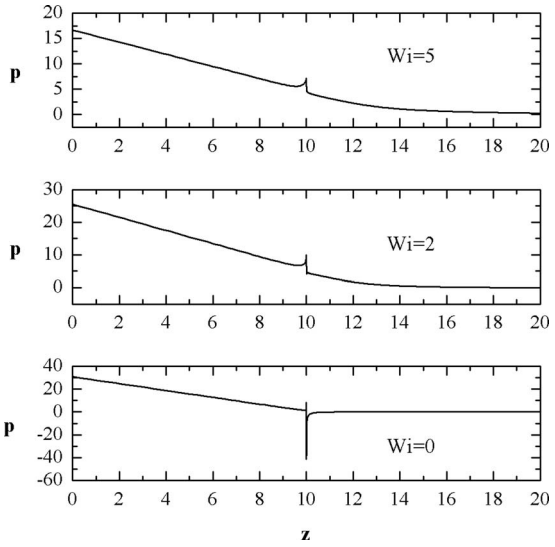

FIG. 15. Dependence of the pressure on z along the die wall and the free surface of the fluid as a function of Wi for $\varepsilon=0.02$, $\beta=0$, $l_1=10$, $l_2=50$. Planar die, mesh M4.

The overshoot in v_z can be seen more clearly in Fig. 14 to display larger maximum values as fluid elasticity increases. Additionally, it is observed that increasing fluid elasticity delays the increase in v_z downstream from the die exit. This behavior is in complete contrast to the Newtonian case where the variation of both v_z and v_r are monotonic in the z-direction. In similar profiles studying the effect of the solvent viscosity ratio, it is found that when β increases, decreasing fluid elasticity, the maximum value of v_z decreases and it moves to larger values of z. Similar is the effect of decreasing the ε parameter of the PTT model.[30]

The variation of pressure is shown on the upper half of Figs. 12(b) and 13(b). Inside the die, the pressure varies almost linearly along the z-direction, the main flow direction, with almost no dependence on the r-direction except for a region around the die lip, where the flow becomes two dimensional. We should note here that although the pressure for a Newtonian fluid decreases abruptly near the triple contact point[16] because of the singularity, this is not observed in the case of the viscoelastic fluid where its variation seems to be smoother. This is in agreement with the findings of Baaijens.[23] On the lower half of this figure we present the variation of the shear stress, τ_{prz}. We observe that it is nonzero inside the die taking its maximum value at the die lip, while it gradually tends to zero in a distance of about two die gaps. Contour lines of τ_{prr} and τ_{pzz} are depicted on the upper and lower halves, respectively, of Figs. 12(c) and 13(c). The smoothness of the contours (without any kind of postprocessing) testifies to the high quality of the obtained results, still with the M4 mesh. Clearly the variation of τ_{prr} takes place mostly outside the die. Its minimum value arises on the free surface near the die exit while it is maximized at the axis or plane of symmetry about one die gap downstream from the die exit. At the same position τ_{pzz} is minimized. This stress component varies mainly inside the die, assuming its maximum value at the die lip, while it gradually decreases as the fluid exits the die. Both normal stresses exhibit a boundary layer along the slip surface, which starts at the singular point and extends to a long distance downstream, whereas the shear stress varies mainly around the singular point. Similar is the picture of the planar case. Moreover, in Fig. 12(d) one can see the isolines of $\tau_{p\theta\theta}$ (upper half) and the rate of strain (lower half) for the cylindrical die. The azimuthal stress field is divided in two different regions, a compressive one inside the die and an extensive and more intense one outside the die. As for the rate of strain, it takes nonzero values inside the die where we have a shear dominated flow, while outside the die it takes very small values since the flow is becoming shear- and extension-free. Similar to the Newtonian fluid case, all variables assume their extreme values with larger magnitude in the cylindrical geometry.

As we have seen in Figs. 12(b) and 13(b) the variation of pressure is much smoother than in the Newtonian case where the pressure decreases abruptly at the die lip. This can be seen more clearly in Fig. 15 where we depict the variation of the pressure along the die wall and the free surface ($r=1$) for a viscoelastic fluid with $\varepsilon=0.02$, $\beta=0$, and various Weissenberg numbers. Clearly we observe that the pressure for a Newtonian fluid is singular, as expected, and assumes much larger values, while for the viscoelastic PTT fluid the intensity of the singularity decreases. We must note here that setting $\beta=0$ means that there is no Newtonian contribution and the fluid is purely elastic. If we add, however, some Newtonian solvent contribution to the viscoelastic fluid, we

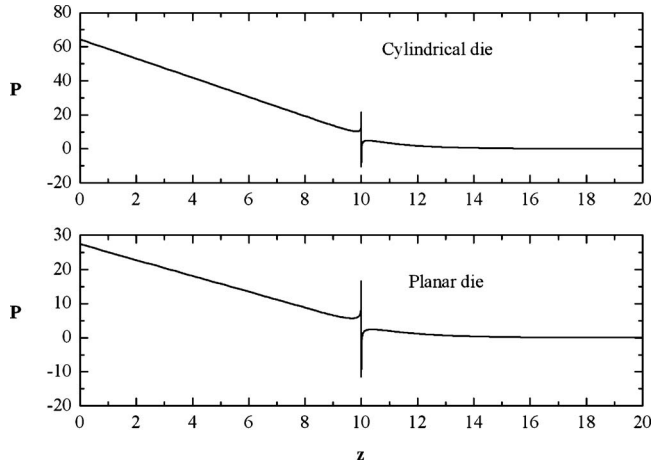

FIG. 16. Dependence of the pressure on z along the die wall and the free surface of the fluid for Wi=2, ε=0.02, β=0.3, l_1=10, and l_2=50, mesh M4.

get a qualitative change in the pressure variation around the singularity. This is shown in Fig. 16, where we have plotted the pressure along r=1 for Wi=5, ε=0.02, and β=0.3. We observe that the intensity of the singularity increases tending to the Newtonian limit as β tends to unity since the more singular Newtonian solvent behavior dominates the elastic one. This concurs with our findings and analysis in Sec. IV C.

The variation of the polymeric stresses along r=1 for Wi=2, ε=0.02, and for various values of the solvent viscosity ratio is shown in Fig. 17. We can see that τ_{prr} starts from zero inside the die and decreases abruptly after the die lip reaching a minimum value, while far from the die it increases tending to zero. We observe, however, that for nonzero values of the solvent viscosity ratio, β, the solution at the die lip presents an oscillation, the size of which increases significantly with β. This is a clear indication that the increase in the solvent viscosity ratio makes the singularity more intense which is in agreement with the results presented in Table V. Moreover, this oscillation is not present for β=0 (see also Fig. 20 below) which indicates that there is a qualitative change in the solution close to the singularity due to the presence of the solvent. This is in agreement with the findings of Salamon *et al.*[21] who also noticed that the partial-slip/slip flow for an Oldroyd-B fluid is dramatically different from that of a UCM fluid because of the presence of the solvent. The variation of τ_{prz}, in contrast to that of the normal stresses, is localized mainly around the die lip and therefore, it is drawn only in the region $9 \le z \le 11$. Indicatively we mention that in the region $10 \le z \le 10.2$ and for the M4 mesh there are 135 elements in the axial direction in order to resolve the flow. Inside the die τ_{prz} is nonzero due to the shear flow whereas outside the die, it becomes zero since the flow is shear-free on the free surface. At the die lip τ_{prz} increases abruptly and its maximum value increases with β due to the increasing intensity of the singularity. As previously observed the axial normal stress assumes the larger magnitudes and, probably, causes the oscillatory variation of both velocity components.

Finally the variation of the exit pressure losses as a func-

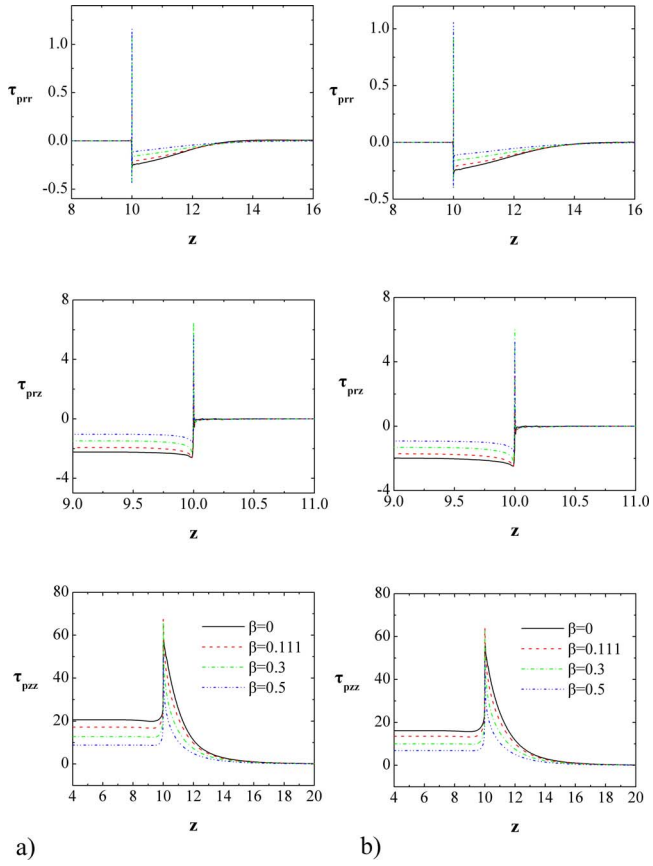

FIG. 17. (Color online) Variation of τ_{prr}, τ_{prz}, and τ_{pzz} along the die wall and the free surface of the fluid as a function of the solvent viscosity ratio for Wi=2, ε=0.02, l_1=10, and l_2=50: (a) cylindrical die and (b) planar die, mesh M4.

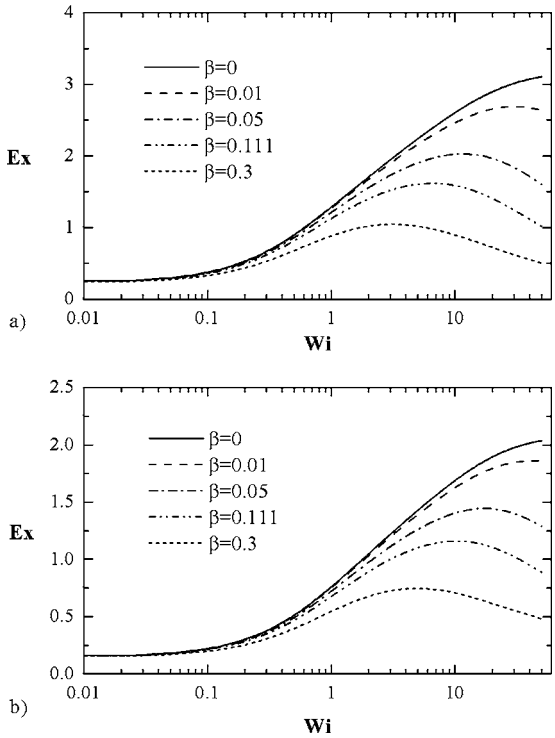

FIG. 18. Dependence of the exit pressure losses on the Wi number for ε=0.05 as a function of the solvent viscosity ratio, β: (a) cylindrical die and (b) planar die, mesh M1.

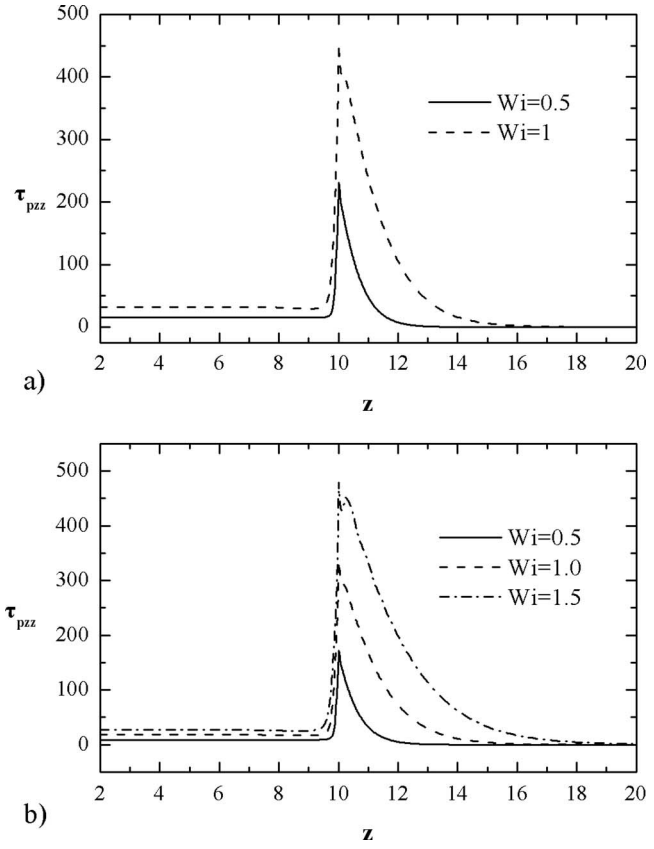

FIG. 19. Variation of τ_{pzz} along the line $r=1$ for a UCM fluid for (a) a cylindrical die and (b) a planar die, mesh M1.

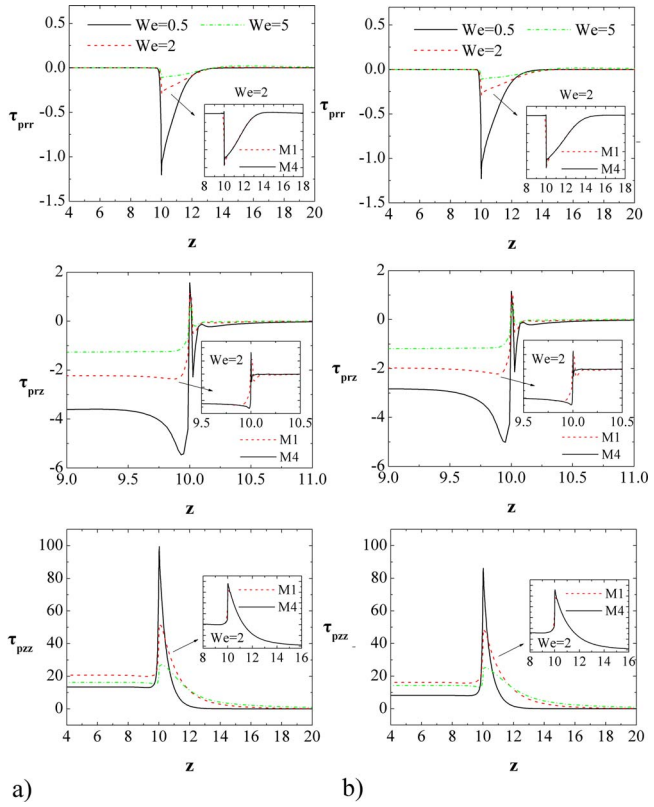

FIG. 20. (Color online) Variation of τ_{prr}, τ_{prz}, and τ_{pzz} along the die wall and the free surface of the fluid as a function of Wi for $\varepsilon=0.02$, $\beta=0$, $l_1=10$, and $l_2=50$: (a) cylindrical die and (b) planar die, mesh M1. Inserted figures show comparison of the solution using meshes M1 and M4 for Wi=2.

tion of Wi for various values of the solvent viscosity ratio and for $\varepsilon=0.05$ is shown in Fig. 18. We observe that for all values of β the pressure losses initially increase with Wi while for larger Wi values, where the effect of the elasticity of the fluid has saturated, it decreases significantly because the effect of shear thinning has taken over. Generally, the maximum value of ex decreases as β increases and the fluid tends to the Newtonian limit.

Another important factor of the PTT model is the extensional parameter, ε. While this parameter imposes an upper limit on the elongational viscosity, which varies inversely with it, this parameter is also related to its shear-thinning behavior. Setting ε equal to zero, the PTT model reduces to the well known Oldroyd-B model, which predicts no shear thinning as well as an infinite extensional viscosity for the fluid. We performed simulations using the UCM model ($\varepsilon=\beta=0$) which however stopped at relatively low Weissenberg number ($\mathrm{Wi}_{\mathrm{lim}}=1.1$ for the cylindrical and $\mathrm{Wi}_{\mathrm{lim}}=1.8$ for the planar die), as in Refs. 19 and 20. Figure 19 shows the axial normal stress along the die wall and the free surface, $r=1$, for various Weissenberg numbers. The infinite extensional viscosity that the UCM model predicts, results in very high values of τ_{pzz} around the die lip, which grow rapidly with Wi causing probably the failure of our calculations at even larger Wi numbers. We should note here that we found no such limitation for Wi when we used the PTT model. The polymeric stresses for such a case are depicted in Fig. 20 along $r=1$ for $\varepsilon=0.02$, $\beta=0$, and various Wi. More specifically we find that the magnitude of the maximum value of the normal stresses now decreases with the increase in Wi because increasing the latter parameter decreases the extensional viscosity and simultaneously increases shear thinning. In addition, shear thinning makes the transition of τ_{prz} from the no-slip region at the die wall to the slip surface, smoother as Wi increases. The calculations shown in this figure were done using our coarsest mesh M1. Comparing the solution with the one using mesh M4 shows (see figures in the inset of Fig. 20) that the solution is almost identical. In order to show the effect of the elongation parameter of the PTT model, ε, the polymeric stresses are depicted in Fig. 21 for a given Weissenberg number and solvent viscosity ratio (Wi=2 and $\beta=0$). The figure in the inset shows a comparison of the solution using meshes M1 and M4 for $\varepsilon=0.05$. We observe that the magnitude of the minimum value of τ_{prr} remains roughly the same, while its dependence in the z-direction has changed significantly. Inside the die the value of τ_{pzz} as well as its maximum value outside it decreases significantly with ε due to the decreased elongational viscosity and the increased shear thinning. In general, all stress components vary less abruptly as ε increases. Indeed these results are in agreement with the analytical works presented by Renardy[38,39] who showed that the elastic stresses for a PTT fluid near a re-entrant corner are less singular than Newtonian stresses, whereas the boundary layers near the walls are much less sharp than for the UCM fluid.

Finally the variation of the exit pressure loss is examined

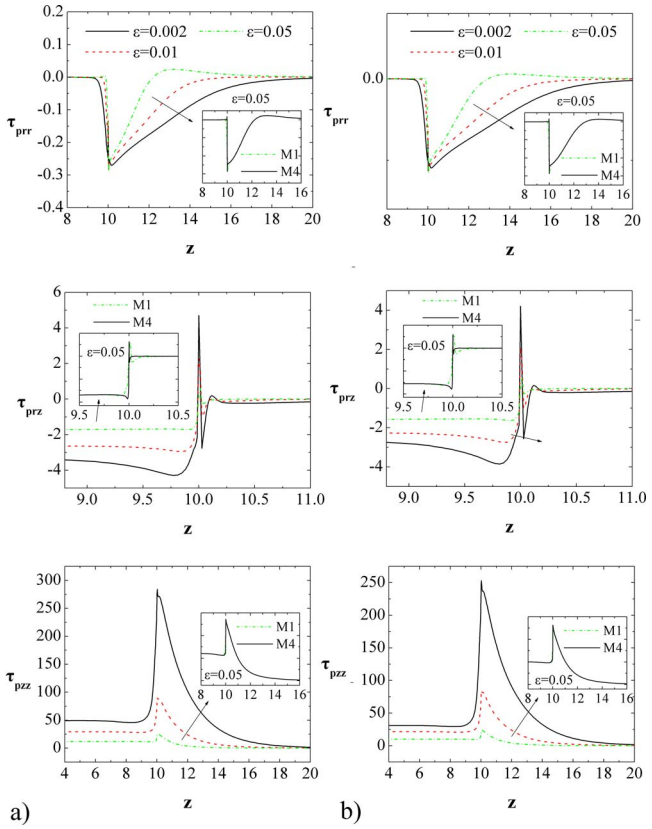

FIG. 21. (Color online) Variation of τ_{prr}, τ_{prz}, and τ_{pzz} along the die wall and the free surface of the fluid as a function of the elongation parameter, ε for Wi=2, β=0, l_1=10, and l_2=50: (a) cylindrical die and (b) planar die, mesh M1. Inserted figures show comparison of the solution using meshes M1 and M4 for ε=0.05.

as a function of Wi and for various values of the extensional parameter, ε, but not plotted here for conciseness, see Ref. 30. It is found that the pressure losses initially increase with Wi, while they tend to level out for large Wi values. Moreover, the pressure losses decrease with the increase in the extensional parameter because of the increased shear thinning that this parameter introduces to the PTT model.

V. CONCLUSIONS

The purpose of this work was to elucidate the predictions of the PTT fluid model in the stick-slip flow for either a cylindrical or a planar geometry. In order to achieve this we first performed numerical simulations for the steady stick-slip flow for a Newtonian fluid to verify the accuracy of our predictions in this limit. In this case the numerical calculations were performed with two different types of elements at the singular point (OFEM and SFEM). Our Newtonian calculations were in very good agreement with the results presented already in literature. For our viscoelastic simulations only OFEMs were used in combination with the EVSS-G method for the calculation of the elastic stresses and the SUPG method for the weighting of the constitutive equation. This was done so that the global Jacobian matrix of all variables is generated which is needed for studying the stability of this flow. We verified the convergence of our simulations for the PTT model with mesh refinement to predictions reported earlier. Subsequently, we presented a thorough study on the form of the singularity that arises at the die lip. It is shown that the singularity for the case of a PTT fluid becomes less intense than for a Newtonian one, which ensures the integrability of all the calculated variables. It is found that the intensity of the singularity does not depend on the Weissenberg number whereas this is not always true for the elongational parameter, ε, as the flow field seems to be affected when ε takes very small values. On the other hand, the addition of solvent viscosity has a significant effect on the intensity of the singularity as the flow field around the die lip tends to the Newtonian limit. Moreover, our calculations show that the structure of the solution is different for β=0 from that predicted for finite values of the solvent viscosity. These findings are in agreement with earlier numerical and analytical works. In most of the latter, however, the assumption of a Newtonian velocity field is usually made which is shown here that is not accurate for a viscoelastic fluid. Finally, a parametric analysis was presented for the viscoelastic steady stick-slip flow. The selected fluid model and solution methodology allowed convergence up to very high Weissenberg numbers. We examined the effect of the elasticity, the extensional parameter, ε, which is related to the shear-thinning behavior of the fluid, as well as the effect of the Newtonian solvent contribution on this flow. We found that for a PTT fluid the elastic stresses decrease with the increase in Wi, while the variation of pressure around the singularity becomes smoother. This is opposite to the predictions using a UCM fluid model, where the stresses increase without bound even for small increases in Wi. This trend very soon leads to the failure of the UCM model.

ACKNOWLEDGMENTS

The comments of one referee, which led us to pursue a much finer mesh to resolve the singularity at the die exit, are thankfully acknowledged.

[1] C. J. S. Petrie and M. M. Denn, "Instabilities in polymer processing," AIChE J. **22**, 209 (1976).
[2] M. M. Denn, "Issues in viscoelastic fluid mechanics," Annu. Rev. Fluid Mech. **22**, 13 (1990).
[3] M. M. Denn, "Extrusion instabilities and wall slip," Annu. Rev. Fluid Mech. **33**, 265 (2001).
[4] R. G. Larson, "Instabilities in viscoelastic flows," Rheol. Acta **31**, 213 (1992).
[5] N. Phan-Thien and R. I. Tanner, "A new constitutive equation derived from network theory," J. Non-Newtonian Fluid Mech. **2**, 353 (1977).
[6] N. Phan-Thien, "A nonlinear network viscoelastic model," J. Rheol. **22**, 259 (1978).
[7] R. Natarajan and A. Acrivos, "The instability of the steady flow past sphere and disks," J. Fluid Mech. **254**, 323 (1993).
[8] M. D. Smith, Y. L. Joo, R. C. Armstrong, and R. A. Brown, "Linear stability analysis of flow of an Oldroyd-B fluid through a linear array of cylinders," J. Non-Newtonian Fluid Mech. **109**, 13 (2003).
[9] S. Richardson, "A 'stick-slip' problem related to the motion of a free jet at low Reynolds numbers," Proc. Cambridge Philos. Soc. **67**, 477 (1970).
[10] D. B. Ingham and M. A. Kelmanson, *Boundary Integral Equation Analyses of Singular, Potential, and Biharmonic Problems* (Springer-Verlag, Berlin, 1984), pp. 21–51.
[11] G. C. Georgiou, L. G. Olson, W. W. Schultz, and S. Sagan, "A singular finite element for stokes flow: The stick-slip problem," Int. J. Numer. Methods Fluids **9**, 1353 (1989).
[12] R. I. Tanner and X. Huang, "Stress singularities in non-Newtonian stick-slip and edge flows," J. Non-Newtonian Fluid Mech. **50**, 135 (1993).

[13]S. A. Trogdon and D. D. Joseph, "The stick-slip problem for a round jet I. Large surface tension," Rheol. Acta **19**, 404 (1980).
[14]D. H. Michael, "The separation of a viscous liquid at a straight edge," Mathematika **5**, 82 (1958).
[15]H. K. Moffatt, "Viscous and resistive eddies near a sharp corner," J. Fluid Mech. **18**, 1 (1964).
[16]T. R. Salamon, D. E. Bornside, R. C. Armstrong, and R. A. Brown, "The role of surface tension in the dominant balance in the die swell singularity," Phys. Fluids **7**, 2328 (1995).
[17]C. J. Coleman, "On the use of boundary integral methods in the analysis of non-Newtonian fluid flow," J. Non-Newtonian Fluid Mech. **16**, 347 (1984).
[18]J. M. Marchal and M. J. Crochet, "A new mixed finite element for calculating viscoelastic flow," J. Non-Newtonian Fluid Mech. **26**, 77 (1987).
[19]J. Rosenberg and R. Keunings, "Numerical integration of differential viscoelastic models," J. Non-Newtonian Fluid Mech. **39**, 269 (1991).
[20]R. G. Owens and T. N. Phillips, "A spectral domain decomposition method for the planar non-Newtonian stick-slip problem," J. Non-Newtonian Fluid Mech. **41**, 43 (1991).
[21]T. R. Salamon, D. E. Bornside, R. C. Armstrong, and R. A. Brown, "Local similarity solutions for the stress field of an Oldroyd-B fluid in the partial-slip/slip flow," Phys. Fluids **9**, 2191 (1997).
[22]A. Fortin, A. Zine, and J.-F. Agassant, "Computing viscoelastic fluid flow problems at low cost," J. Non-Newtonian Fluid Mech. **45**, 209 (1992).
[23]F. P. T. Baaijens, "Application of low-order discontinuous Galerkin methods to the analysis of viscoelastic flows," J. Non-Newtonian Fluid Mech. **52**, 37 (1994).
[24]V. Ngamaramvaranggul and M. F. Webster, "Viscoelastic simulations of stick-slip and die-swell flows," Int. J. Numer. Methods Fluids **36**, 539 (2001).
[25]D. Rajagopalan, R. C. Armstrong, and R. A. Brown, "Finite element methods for calculation of steady, viscoelastic flow using constitutive equations with Newtonian viscosity," J. Non-Newtonian Fluid Mech. **36**, 159 (1990).
[26]R. A. Brown, M. J. Szady, P. J. Northey, and R. C. Armstrong, "On the numerical stability of mixed finite-element methods for viscoelastic flows governed by differential constitutive equations," Theor. Comput. Fluid Dyn. **5**, 77 (1993).
[27]D. O. Cruz, A. Pinho, and F. T. Oliveira, "Analytical solutions for fully developed laminar flow of some viscoelastic liquids with a Newtonian solvent contribution," J. Non-Newtonian Fluid Mech. **132**, 28 (2005).
[28]M. Pavlidis, Y. Dimakopoulos, and J. Tsamopoulos, "Fully developed flow of a viscoelastic film down a vertical cylindrical or planar wall," Rheol. Acta **48**, 1031 (2009).
[29]A. N. Brooks and T. J. R. Hughes, "Streamline upwind/Petrov-Galerkin formulations for convection dominated flows with particular emphasis on the incompressible Navier-Stokes equations," Comput. Methods Appl. Mech. Eng. **32**, 199 (1982).
[30]G. Karapetsas, "A study on time-dependent and unstable under conditions flows of viscoplastic and viscoelastic fluids," Ph.D. thesis, University of Patras, 2007.
[31]N. Chatzidai, A. Giannousakis, Y. Dimakopoulos, and J. Tsamopoulos, "On the elliptic mesh generation in domains containing multiple inclusions and undergoing large deformations," J. Comput. Phys. **228**, 1980 (2009).
[32]T. J. Chung, *Computational Fluid Dynamics* (Cambridge University Press, Cambridge, 2002), pp. 533–580.
[33]G. Karapetsas and J. Tsamopoulos, "Steady extrusion of viscoelastic materials from an annular die," J. Non-Newtonian Fluid Mech. **154**, 136 (2008).
[34]O. Schenk and K. Gärtner, "Solving unsymmetric sparse systems of linear equations with PARDISO," FGCS, Future Gener. Comput. Syst. **20**, 475 (2004).
[35]O. Schenk and K. Gärtner, "On fast factorization pivoting methods for symmetric indefinite systems," Electron Trans. Numer. Anal. **23**, 158 (2006).
[36]M. Elliotis, G. Georgiou, and C. Xenophontos, "Solution of the planar Newtonian stick-slip problem with the singular function boundary integral method," Int. J. Numer. Methods Fluids **48**, 1001 (2005).
[37]K. B. Broberg, *Cracks and Fracture* (Academic, San Diego, 1999), pp. 63–66.
[38]M. Renardy, "The stresses of an upper convected Maxwell fluid in a Newtonian velocity field near a re-entrant corner," J. Non-Newtonian Fluid Mech. **50**, 127 (1993).
[39]M. Renardy, "Re-entrant corner behaviour of the PTT fluid," J. Non-Newtonian Fluid Mech. **69**, 99 (1997).
[40]E. J. Hinch, "The flow of an Oldroyd fluid around a sharp corner," J. Non-Newtonian Fluid Mech. **50**, 161 (1993).
[41]J. D. Evans and D. N. Sibley, "Re-entrant corner flow for PTT fluids in the Cartesian stress basis," J. Non-Newtonian Fluid Mech. **153**, 12 (2008).
[42]J. D. Evans and D. N. Sibley, "Re-entrant corner flow for PTT fluids in the natural stress basis," J. Non-Newtonian Fluid Mech. **157**, 79 (2009).
[43]R. Keunings, "On the high Weissenberg number problem," J. Non-Newtonian Fluid Mech. **20**, 209 (1986).
[44]T. Hagen and M. Renardy, "Boundary layer analysis of the Phan-Thien-Tanner and Giesekus model in high Weissenberg number flow," J. Non-Newtonian Fluid Mech. **73**, 181 (1997).